Corollary Discharge Promotes a Sustained Motor State in a Neural Circuit for Navigation

Ni Ji[1†], Vivek Venkatachalam[1‡], Hillary Rodgers[1,3], Wesley Hung[2], Taizo Kawano[2], Christopher M. Clark[3], Maria Lim[2], Mark J. Alkema[3*], Mei Zhen[2*], Aravinthan D.T. Samuel[1*]

*For correspondence:
mark.alkema@umassmed.edu (MA);
zhen@lunenfeld.ca (MZ);
samuel@physics.harvard.edu (ADTS)

Present address: [†]Department of Brain and Cognitive Sciences, MIT, Cambridge, MA USA; [‡]Department of Physics, Northeastern University, Boston, MA USA

[1]Department of Physics and Center for Brain Science, Harvard University, 17 Oxford Street, Cambridge, MA 02138 USA; [2]Lunenfeld-Tanenbaum Research Institute, Mount Sinai Hospital, Toronto, ON, Canada M5G 1X5; and Departments of Molecular Genetics, and Physiology, University of Toronto, Toronto, ON, Canada M5S 1A8; [3]Department of Neurobiology, University of Massachusetts Medical School, Worcester, MA USA

Abstract Animals exhibit behavioral and neural responses that persist on longer time scales than transient or fluctuating stimulus inputs. Here, we report that *C. elegans* uses feedback from the motor circuit to a sensory processing interneuron to sustain its motor state during thermotactic navigation. By imaging circuit activity in behaving animals, we show that a principal postsynaptic partner of the AFD thermosensory neuron, the AIY interneuron, encodes both temperature and motor state information. By optogenetic and genetic manipulation of this circuit, we demonstrate that the motor state representation in AIY is a corollary discharge signal. RIM, an interneuron that is connected with premotor interneurons, is required for this corollary discharge. Ablation of RIM eliminates the motor representation in AIY, allows thermosensory representations to reach downstream premotor interneurons, and reduces the animal's ability to sustain forward movements during thermotaxis. We propose that feedback from the motor circuit to the sensory processing circuit underlies a positive feedback mechanism to generate persistent neural activity and sustained behavioral patterns in a sensorimotor transformation.

Introduction

Animals are able to generate behaviors that persist beyond the timescales of the inciting sensory stimuli. For example, fish continue to fixate their gaze after the onset of darkness (*Seung, 1996*; *Aksay et al., 2007*). A brief aversive stimulus can evoke prolonged escape responses in many species (*Li et al., 2006*; *Herberholz et al., 2002*). Lasting behavioral states require circuit mechanisms to turn a transient stimulus into persistent neuronal activity (*Lee and Dan, 2012*; *Major and Tank, 2004*; *Inagaki et al., 2019*; *Kennedy et al., 2020*). Theoretical studies have explored roles for recurrent circuitry, in particular positive feedback, in generating persistent neural activity (*Seung, 1996*). While recurrent connections are abundant in the brain, establishing causality between recurrent circuitry, persistent neural activity, and sustained behavior states has been challenging in part due to the technical difficulties in experimentally dissecting neural dynamics across entire sensorimotor pathways.

One type of recurrent connectivity that is widely observed across phyla are neuronal projections that convey motor-related signals to brain regions for sensory processing (*Wurtz, 2018*; *Crapse and*

Sommer, 2008). These signals, called corollary discharge (CD) or efference copy (EC), were first pro-posed (*Sperry, 1950*; *Holst and Mittelstaedt, 1950*) and subsequently demonstrated (*Poulet and Hedwig, 2002*; *Requarth and Sawtell, 2014*; *Schneider et al., 2014*; *Kim et al., 2015*) as mechanisms to cancel sensory reafferents generated by self-motion. Recent studies, however, have also identi-fied examples of motor-to-sensory feedback that are excitatory (*Hendricks, 2012*; *Lee et al., 2013*; *Zagha et al., 2013*; *Fu et al., 2014*). Emerging evidence from cortex- or brain-wide activity patterns has revealed widespread representation of motor states in sensory processing regions (*Kato et al., 2015*; *Stringer et al., 2019*; *Aimon et al., 2019*; *Musall et al., 2019*; *Marques et al., 2020*), which is likely to be caused, at least in part, by motor-to-sensory feedback. These observations suggest diverse roles for CD in sensorimotor processing.

The compact nervous system and optical accessibility of *C. elegans* make it possible to explore circuit mechanisms that underlie sustained behavioral states in intact animals (*Gao et al., 2015*). *C. elegans* requires persistent motor states to navigate variable sensory environments. During loco-motion, the animal alternates between continuous forward movements (runs) and brief backward movements (reversals). When navigating through a chemical or thermal gradient, *C. elegans* em-ploys a biased random walk strategy, selectively extending forward runs when moving along pre-ferred directions and shortening runs when veering off course (*Pierce-Shimomura et al., 1999*; *Ryu and Samuel, 2002*; *Ino and Yoshida, 2009*; *Hedgecock and Russell, 1975*; *Mori and Ohshima, 1995*; *Luo et al., 2014a*). During forward runs, *C. elegans* also gradually steers its heading angle towards the preferred direction, a strategy called klinotaxis (*Ward, 1973*; *Ino and Yoshida, 2009*). Forward runs play a crucial role in *C. elegans* navigation, but the neural circuit basis for run persistence remains poorly understood.

Here, we study the sensorimotor pathway that controls navigation towards warmer tempera-tures (positive thermotaxis). Past studies have revealed a multi-layered neural circuit underlying this behavior. AFD is the thermosensory neuron that mediates both positive and negative ther-motaxis (*Luo et al., 2014a*; *Hawk et al., 2018*). Its principal chemical synaptic partner, AIY, is a first-layer interneuron specifically required for positive thermotaxis. AIY responds to temperature variations due to excitatory input from AFD (*Clark et al., 2006*; *Narayan et al., 2011*; *Hawk et al., 2018*). AIY sends synaptic outputs to multiple second-layer interneurons, which in turn synapse onto head motor neurons and premotor interneurons that drive forward runs or reversals. AIY has been shown to promote the speed and duration of forward locomotion (*Li et al., 2014*; *Tsalik and Hobert, 2003*). AIY is also postsynaptic to multiple other sensory neurons, and is thought to play a role in navigation across different sensory modalities by controlling run duration (*Gray et al., 2005*; *Wakabayashi et al., 2004*; *Tsalik and Hobert, 2003*).

We probed mechanisms by which AIY biases random walks during positive thermotaxis. Imag-ing AIY activity in moving animals reveals that AIY encodes both temperature and motor informa-tion. Previous studies have found AIY to encode either sensory stimuli (*Chalasani et al., 2008*; *Clark et al., 2006*) or locomotory state (*Li et al., 2014*; *Luo et al., 2014b*) in different experimental paradigms. Here, we found that thermosensory response in AIY is gated by the locomotory state of the animal. In the absence of thermosensory stimuli, AIY activity reliably encodes the locomotory state. When exposed to thermal fluctuations during forward runs, AIY activity exhibits variability but tends to be excited by warming and inhibited by cooling. During reversals, AIY activity remains low and does not encode thermal stimuli.

We demonstrate that the motor state encoding in AIY represents a corollary discharge (CD) signal from premotor interneurons that drive the forward run and reversal states. This CD signal requires RIM, an interneuron that is connected with premotor interneurons. In the absence of RIM, AIY activity reliably encodes thermal stimuli regardless of the locomotory state. Loss of RIM also leads to increased thermosensory representation in premotor interneurons and motor neurons. At the behavioral level, loss of RIM led to defects in positive thermotaxis by reducing the persistence of the forward run state. Our results establish a role for corollary discharge in sustaining a motor state in variable or fluctuating sensory environments.

Results

Forward movements are sustained across thermal fluctuations during positive thermotaxis

C. elegans navigates towards temperatures that correspond to prior thermal experience. To evoke positive thermotaxis, we placed young adults cultivated at 25°C on a linear thermal gradient spanning 19 to 23°C (*Figure 1*). Consistent with earlier reports, these animals exhibited biased random walk and klinotaxis towards warmer temperatures (*Figure 1B*) (*Luo et al., 2014a*; *Yamaguchi et al., 2018*): runs that pointed in favorable directions were lengthened (*Figure 1B*; forward heading angles gradually reoriented towards temperatures that correspond to prior experience (*Figure 1B*). Without a temperature gradient, there was no evident modulation of either run length or heading angle (*Figure 1B*).

Individual trajectories during positive thermotaxis revealed periods of forward movement that carry the animal up the temperature gradient. Although these periods of forward movement are persistent in duration, they are not always persistent in direction (*Figure 1C*; *Figure 1–Figure Supplement 1*). *C. elegans* experiences temporal changes in temperature on spatial gradients because of its own movements. Most runs – even those that orient the animal towards warmer temperatures – will involve periods of both warming and cooling stimuli because of frequent changes in movement direction (*Figure 1D*; *Figure 1–Figure Supplement 1*). Thus, *C. elegans* reveals an ability to sustain forward movement up temperature gradients despite transient cooling fluctuations.

Thermosensory representation in AIY is gated by the motor state

To uncover circuit mechanisms for sustaining forward movement against thermal fluctuations, we simultaneously imaged the calcium activity across a group of neurons involved in thermosensory processing, locomotory control, or both. These include the principal thermosensory neuron AFD, its primary postsynaptic partner AIY, the premotor interneuron AVA, the left-right pair of the head motor neurons RME, SMDV and SMDD, and the RIM interneuron that extensively connects with premotor interneurons and motor neurons (*Figure 2A,B*). To measure locomotory behavior while minimizing motion artifact, we performed imaging in semi-constrained animals that exhibited sinusoidal movements akin to those observed in free-moving animals (*Figure 2–Figure Supplement 1*, also see **Methods**). This approach allowed us to simultaneously examine the encoding of thermosensory and motor information in the same neurons.

First, we measured the activity of the AFD thermosensory neuron and AIY, its principal postsynaptic partner, by calcium imaging in moving animals. Subjected to oscillating temperatures below the preferred temperature, *C. elegans* exhibits positive thermotaxis. As previously reported (*Clark et al., 2006*, *2007*), AFD's activity phase locks to periodic variations in temperatures, rising upon warming and falling upon cooling (*Figure 2C,D*). AFD activity did not covary with transitions between forward run and reversal states (*Figure 2C*), indicating that motor commands arise downstream of the thermosensory neuron.

Next, we simultaneously monitored AIY calcium dynamics along with components of the motor circuit known to code forward and reversal motor states (*Figure 2A,B*, *Figure 1-Videos 1 and 2*). We found that AIY encodes both temperature variations in a motor state dependent manner. During forward movements, AIY's calcium activity on average increased upon warming and decreased upon cooling with substantial trial-to-trial variability (*Figure 2E-G*). During reversals, these responses were largely absent (*Figure 2E*).

Unlike AFD and AIY, all motor circuit neurons that we examined exhibited little to no phase-locked response to thermosensory stimulation. Instead, motor neurons reliably encoded the forward versus reversal movement states (*Figure 2E,F*, see the stimulus cross-correlation plots). In animals subjected to oscillating thermosensory stimulation, AVA calcium activity exhibited high and low states that correlated with backward and forward movement, respectively (*Figure 2E*). This observation is consistent with the known activity profile of AVA in the absence of thermal stimulation

141 and its functional role in promoting the reversal state (*Chalfie et al., 1985*; *Kawano et al., 2011*;
142 *McCormick et al., 2011*; *Kato et al., 2015*). Similarly, the RIM interneuron was selectively active
143 during reversals and its activity positively correlated with AVA activity. The head motor neurons
144 RME, SMDD, and SMDV were selectively active during forward runs. The SMD neurons exhibited
145 alternating activity patterns, consistent with previous reports (*Hendricks, 2012*). Together, these
146 observations indicate that, for positive thermotaxis, the sensorimotor transformation progresses
147 through three layers of processing (*Figure 2A*): the thermosensory neuron encodes only thermal
148 stimuli; the first layer interneuron encodes both thermal stimuli and motor states; the premotor
149 and motor neurons primarily encode the motor state.

150 To elucidate which of these activity patterns are driven by thermosensory inputs, we next mea-
151 sured the activity of these neurons under constant temperature (*Figure 2H*). We found that the
152 activity of all six neurons continued to be modulated by locomotory state in the same way as when
153 exposed to oscillating temperature. Furthermore, the pair-wise cross-correlation between neu-
154 rons remained the same under both oscillatory and constant temperature (*Figure 2I*). Specifically,
155 AIY and RME were positively correlated with one another and were anti-correlated with AVA. The
156 head motor neurons SMDD and SMDV were strongly anti-correlated with one another, consistent
157 with previous reports (*Hendricks, 2012*). Both SMDD and SMDV were positively correlated with
158 RME and AIY, consistent with their role in controlling head oscillations during forward locomotion
159 (*Pirri et al., 2009*). These observations indicate that the widespread encoding of motor state in
160 neurons downstream of AFD does not require thermosensory input and may instead reflect an
161 intrinsic circuit property.

162 **Motor coding in AIY is a corollary discharge signal that requires RIM**
163 Our finding that AIY encodes thermal information in a manner that depends on motor state sug-
164 gests a critical role in sensorimotor transformations during positive thermotaxis. In animals ex-
165 posed to either constant or oscillating temperatures, AIY activity consistently rises at the begin-
166 ning of forward runs and decays at the onset of reversals (*Figure 3A,B*). Moreover, AIY exhibited
167 persistent activation, the duration of which coincided reliably with that of the forward run state
168 (*Figure 3–Figure Supplement 1*). How does AIY, a first order interneuron, acquire a robust motor
169 signal?

170 Because AIY has an established role in promoting forward locomotion, we first tested whether
171 motor representation in AIY arises due to feedforward output from AIY to the downstream circuit.
172 We imaged AIY activity after blocking vesicle release from AIY through cell-specific expression of
173 tetanus toxin (TeTx) (*Figure 3C*). Despite the lack of synaptic and dense-core-vesicle dependent
174 chemical release (*Whim et al., 1997*), AIY activity remained strongly coupled to the motor state,
175 implying that AIY must receive the motor state signal.

176 We explored the possibility that proprioception, elicited by movement itself, underlies the cal-
177 cium response in AIY. We imaged neural activity in AIY and the rest of the thermosensory circuit in
178 immobilized animals under constant temperature. As in moving animals, AIY's activity remained
179 anti-correlated with neurons active during reversals (AVA) and correlated with neurons active dur-
180 ing forward movement (RME and SMDD/V) (*Figure 3–Figure Supplement 2*). Furthermore, aligning
181 AIY activity to the onset and offset of AVA activity revealed average activity patterns similar to that
182 of the motor state representation in moving animals (*Figure 3D,E*). *C. elegans* movement is not
183 required for AIY activity to reflect motor state, arguing against proprioception.

184 We next asked whether AIY receives corollary discharge from neurons that encode the motor
185 command. We imaged AIY activity in moving animals upon ablation of AIY's downstream interneu-
186 rons and premotor interneurons (*Figure 4A*). For interneurons, we focused on AIB and RIM. AIB
187 shares electrical synapses with RIM and the AFD thermosensory neuron (*White et al., 1986*). In the
188 context of chemotaxis, AIB and RIM have been shown to regulate variability in the neuronal and
189 behavioral response to olfactory inputs (*Gordus et al., 2015*). We also tested AVA and AVB, pre-
190 motor interneurons that regulate reversal and forward movement, respectively. Ablations were

191 performed by expressing flavoprotein miniSOG, which induces acute functional loss and neuronal
192 death by photoactivation (*Qi et al., 2012*).

193   We found that ablating AIB did not abolish the motor state representation in AIY (*Figure 4A,B*).
194 Neither did the removal of the premotor interneurons AVA or AVB alone (*Figure 4A*, *Figure 4–Figure*
195 *Supplement 1A,B*). However, AIY lost its motor state representation when we ablated RIM, either
196 by itself or in combination with other premotor interneurons (*Figure 4A,B*, *Figure 4–Figure Supple-*
197 *ment 1C*).

198   RIM activity has been shown to be correlated with the AVA premotor interneuron that pro-
199 motes reversals and anti-correlated with the AVB premotor interneuron that promotes forward
200 runs (*Kawano et al., 2011*; *Gordus et al., 2015*; *Kato et al., 2015*). RIM has been shown to promote
201 long reversals (*Gray et al., 2005*) and to suppress head oscillations during reversals (*Alkema et al.,*
202 *2005*). A recent study demonstrated that RIM also promotes the stability of forward runs when
203 hyperpolarized (*Sordillo et al., 2021*). To probe whether RIM is required for the motor state signal
204 to appear in AIY, we optogenetically activated either AVA or AVB while simultaneously measuring
205 AIY calcium activity in immobilized animals. Activation of AVB triggered an increase in AIY calcium
206 levels (*Figure 4C,D*). Activation of AVA using the light-gated opsin chrimson (*Klapoetke et al., 2014*)
207 triggered a decrease in AIY calcium levels (*Figure 4E,F*). When RIM was ablated, AIY calcium signals
208 no longer responded to optogenetic activation of either AVA or AVB, suggesting that RIM is part
209 of the CD pathway from the motor circuit to AIY. Without RIM, AIY activity no longer reflected or
210 depended on the motor state, but the premotor interneurons AVA continued to encode the back-
211 ward and forward movement, albeit with reduced bimodal activity (*Figure 5A,C*). Thus, RIM is not
212 essential for generating motor commands, but is necessary to relay motor information to AIY, a
213 first layer interneuron.

RIM-mediated corollary discharge does not depend on chemical synaptic transmission

216 We sought synaptic mechanisms by which RIM may contribute to the corollary discharge (CD) path-
217 way. RIM expresses VGLUT3/EAT-4, indicating the potential involvement of glutamatergic synaptic
218 transmission (*Serrano-Saiz et al., 2013*). RIM also synthesizes tyramine, a monoamine neuromod-
219 ulator (*Alkema et al., 2005*). We thus imaged AIY activity in loss-of-function mutants for gluta-
220 matergic signaling (*VGLUT3/eat-4*), tyramine synthesis (*TDC/tdc-1*), vesicular monoamine transport
221 (*VMAT/cat-1*) and peptidergic signaling (*CAPS/unc-31*). AIY activity co-varied with the motor state in
222 all mutants, but the difference in AIY activity between the forward run and reversal states was
223 less distinct in mutants defective for vesicular monoamine transport (*VMAT/cat-1*) or tyramine syn-
224 thesis (*TDC/tdc-1*) (*Figure 4–Figure Supplement 2A,B*). Blocking vesicle fusion in RIM by expressing
225 TeTx (P*tdc-1::TeTx*) also attenuated the motor state representation in AIY (*Figure 4–Figure Supple-*
226 *ment 2A,B*).

227   Since perturbation of chemical synaptic transmission did not fully abolish motor-related activity
228 in AIY, neuronal communication that is independent of classic chemical synaptic transmission is
229 likely involved in relaying corollary discharge to AIY. As previously reported (*Kawano et al., 2011*;
230 *Kato et al., 2015*; *Gordus et al., 2015*), RIM activity is strongly correlated with the AVA premotor
231 interneuron, higher during reversals and lower during forward movement. AIY, on the other hand,
232 exhibits increased activity during forward movement (*Figure 3*). This sign reversal may be explained
233 by an inhibitory input from RIM to AIY. Alternatively, RIM may play a permissive role in allowing the
234 motor-related feedback to AIY. Taken together, our results suggest that the joint representation of
235 sensory and motor signals in AIY arises from separate sources: feedforward input from AFD and
236 feedback from the motor circuit that is dependent on RIM.

RIM-dependent corollary discharge promotes persistent forward states and more effective thermotaxis

RIM plays a critical role in the motor state dependent modulation of AIY calcium activity. This prompted us to examine the effect of disrupting the CD signal on sensorimotor transformations. When RIM-ablated animals were subjected to oscillating temperatures, AIY activity was no longer coupled to the motor state, but instead reliably tracked temperature fluctuations during both forward and backward movements (*Figure 5A,B*, *Figure 5-S1A,B*, *Figure 5-Video 3*). Under oscillating temperature, the average duration of AIY activation was shortened compared to wild type, though no significant difference was observed under constant temperature (*Figure 5D*).

When RIM was ablated, we were also able to detect the representation of thermosensory oscillations in the activity pattern of the AVA premotor interneuron and the head motor neurons RME and SMDV (*Figure 5A*). This observation suggests that the loss of the RIM-dependent motor signal resulted in a sensorimotor circuit that becomes more susceptible to fluctuations in thermosensory input. Without RIM and the motor state encoding in AIY, fluctuations in thermosensory inputs are readily propagated to the the motor circuit. Thus, the RIM-dependent CD may play an important role in sustaining neural activity states through fluctuating sensory inputs.

We tested this hypothesis by examining the effect of RIM ablation on positive thermotaxis (*Figure 6A*, *Figure 6–Figure Supplement 1A*). Compared to wild type animals, RIM ablated animals exhibited an overall reduction in thermotaxis bias (*Figure 6B*). These animals were specifically defective in their ability to sustain forward locomotion when moving up the thermal gradient, while their ability to gradually modify heading angle during a forward run remained intact (*Figure 6C*, *Figure 6–Figure Supplement 1A*). At constant temperature, run durations are similar between wild type and RIM ablated animals (*Figure 6–Figure Supplement 1B*). Thus, the loss of RIM specifically disrupted the animal's ability to sustain forward runs up temperature gradients.

If RIM-dependent motor feedback serves to filter out transient thermal fluctuations during positive thermotaxis, then loss of RIM should render the forward run state more susceptible to thermal variations. To test this prediction, we analyzed how periods of cooling affected the forward run state in wild type and RIM ablated animals (*Figure 6D-F*). Overall, cooling induced reversals at a higher probability in RIM ablated animals compared to the wild type. This difference was particularly notable for persistent periods of cooling lasting from 7 to 30 seconds (*Figure 6E*). We also examined the probability with which forward runs end after a period of cooling (*Figure 6–Figure Supplement 1C-E*). We found that, compared to the wild type, forward runs in RIM ablated animals are more likely to end after a period of cooling regardless of run length (*Figure 6–Figure Supplement 1E*). Together, these analyses support a role of the RIM-dependent motor feedback in promoting a persistent forward run state.

Agent-based simulations driven by a reduced model recapitulate the role of CD feedback in positive thermotaxis

To understand how CD might sustain motor states during thermotaxis, we built a minimal dynamical systems model of the thermotaxis circuit (*Figure 7*). In this model, temperature fluctuations encoded by a thermosensory neuron is conveyed to a downstream interneuron. The interneuron then outputs to a motor command neurons that determines the motor state. A copy of the motor command is then relayed back to the interneuron after being weighted by a feedback gain factor (*g*). A positive gain factor means the motor-related signal is reinforcing to the activity of the interneuron, effectively forming a positive feedback loop. A negative gain factor translates to a negative feedback loop. We allowed the gain factor to vary between 1 (positive feedback), 0 (no feedback), and -1 (negative feedback) to test the impact of the recurrent circuit motif on circuit output.

When exposed to oscillating inputs, the positive feedback model exhibited stable high and low states in both the interneuron and the motor neuron. The autocorrelative timescale of these states (a measure of persistence) outlasted the oscillatory period of the input signal (*Figure 7B*). This was

286 not the case for the for models with no feedback or negative feedback where the oscillatory signal
287 remained evident in both the interneuron and the motor neuron (*Figure 7B*).

288 We then used this circuit model to simulate animal locomotion along linear thermal gradients
289 (*Figure 7C*). The positive feedback model more effectively drove migration up the thermal gradient
290 than the model with no feedback. In contrast, the negative feedback model exhibited less effective
291 thermotaxis than the no feedback model (*Figure 7C,D*). The duration of forward runs were overall
292 significantly longer and the exhibited stronger dependence of run duration on run direction in the
293 positive feedback model compared to the alternative models (*Figure 7E*). Lastly, forward runs were
294 much more likely to terminate after a period of cooling in the no feedback model compared to the
295 positive feedback model, consistent with experimental observations in RIM ablated animals. Thus,
296 the positive feedback model best explained the neural activity and behavioral data. These results
297 indicate that CD in the form of positive feedback promotes persistent circuit activity states and
298 effective navigation during time-varying thermosensory inputs.

Discussion

300 We have uncovered a role for corollary discharge, a feedback signal from the motor circuit, in sus-
301 taining a neural state for forward locomotion during *C. elegans* thermotaxis. By relaying a copy of
302 the motor command to a sensory processing interneuron, the thermotaxis circuit encodes a recur-
303 rent loop that integrates rapidly varying thermal inputs with more slowly varying motor state sig-
304 nals. This integration results in stable high and low activity states that sustain the behavioral state
305 corresponding to forward locomotion. Persistent neural activity states may enable the circuit to
306 filter out rapid fluctuations in sensory input and promote efficient navigation in a dynamic sensory
307 environment. During positive thermotaxis up gradients, *C. elegans* becomes better able to sustain
308 periods of forward locomotion that carry it up temperature gradients; CD prevents these periods
309 of forward locomotion from being curtailed by transient negative temperature fluctuations.

310 In mice and flies, recurrent circuitry has a prevalent role in persistent neural activities and be-
311 havioral states. In many systems, CD has a role in suppressing neural or behavioral responses. In
312 contrast, we show that CD is also able to reinforce the behavioral response to a sensory input. In
313 the *C. elegans* circuit for positive thermotaxis, the AIY interneuron receives the motor state signal.
314 Because AIY is postsynaptic to many sensory neurons and is required for navigation in other modal-
315 ities (*Wakabayashi et al., 2004*; *Tsalik and Hobert, 2003*; *Luo et al., 2014a*), CD-based feedback to
316 AIY might play a general role in many different sensorimotor pathways.

317 The RIM interneuron is required for the propagation of the CD signal to AIY to promote posi-
318 tive thermotaxis. In a recent study of olfactory responses in immobilized animals, RIM was also
319 shown to send feedback input to AIB, another sensory processing interneuron whose activity pro-
320 motes the reversal state (*Gordus et al., 2015*). In the olfactory pathway, RIM activity was required
321 to correlate the activity of AIB and the AVA premotor interneuron. Silencing RIM led to more reli-
322 able odor-evoked response in AIB and odor-induced initiation of forward runs. These findings are
323 consistent with a model where a RIM-dependent CD couples AIB activity to the motor command
324 signal, thereby preventing AIB and its downstream circuit from passively responding to fluctuating
325 olfactory inputs. Thus, the effect of silencing RIM in the olfactory sensorimotor pathway mirrors
326 the impact of RIM ablation on AIY, shown in this study, during positive thermotaxis. Together, this
327 evidence suggests a wide role for CD in promoting persistent states in sensorimotor transforma-
328 tion.

329 Our findings add to a growing body of literature from across species that motor behavior can
330 significantly impact sensory processing (*Petreanu et al., 2009*; *Zagha et al., 2013*; *Fu et al., 2014*;
331 *Schneider et al., 2014*; *Seelig and Jayaraman, 2015*; *Ouellette et al., 2018*; *Musall et al., 2019*;
332 *Stringer et al., 2019*; *Salkoff et al., 2020*). An explicit dependence of sensory encoding on behav-
333 ioral states has been shown to contribute to to variability in stimulus-evoked neural and behavioral
334 responses (*Fontanini and Katz, 2008*; *McGinley et al., 2015*). In mice performing visual and auditory
335 tasks, cortex-wide neural activity can be dominated by movement-related signals, many of which

336 are uninstructed (*Musall et al., 2019*). Importantly, these movement-related signals closely predict
337 the inter-trial variability in neural response. In *C. elegans*, whole-brain imaging in both station-
338 ary and moving animals have shown brain-wide encoding of the forward run and reversal states
339 (*Venkatachalam et al., 2016*; *Kato et al., 2015*; *Nguyen et al., 2016*). The roles of the AIY interneu-
340 ron studied here and the AIB interneuron studied in *Gordus et al.* (*2015*) may reflect a general use
341 of the integration of sensory and motor-related signals during *C. elegans* navigation. In both cases,
342 RIM is needed to propagate the motor-related signal to sensory processing interneurons.

343 In addition to its postsynaptic partners predicted by the connectome, RIM releases a diverse
344 array of neuromodulatory signals (*Taylor et al., 2019*). Thus, through RIM and other neurons, the
345 motor state signal may be broadcast to many neuron types, leading to correlated activity patterns
346 throughout the *C. elegans* brain (*Kaplan et al., 2018*). This hypothesis may be tested with whole-
347 brain imaging after RIM inactivation. We do not know the synaptic mechanism by which corollary
348 discharge reaches AIY. We observed that loss of tyramine, a biogenic amine produced by RIM,
349 only partially disrupted the CD signal in AIY. Broadly disrupting biogenic amine synthesis or vesicle
350 release from RIM also yielded similarly partial defects *Figure 4–Figure Supplement 2*.

351 The tyramine receptor, SER-2, is expressed in many neurons including AIY. Cell-specific pertur-
352 bation or rescue of SER-2 function in AIY could help test the requirement of tyramine signaling in
353 relaying the CD signal. Other signaling molecules are likely involved as well, and more extensive
354 molecular and cellular dissection is needed to understand how the CD signal reaches AIY. Inter-
355 estingly, a recent study demonstrated that hyperpolarization of RIM extended the duration of the
356 forward runs during spontaneous locomotion through RIM-specific function of the gap junction
357 protein UNC-9 (*Sordillo et al., 2021*). Exploring the cell-specific involvement of gap junction genes
358 in relaying CD could also elucidate the molecular basis of feedback to AIY.

Methods and Materials
359

Molecular biology and transgenic strain construction
360

361 Promoters
362 The following promoters were used to allow neuron-specific expression of a calcium sensor, chrim-
363 son, and miniSOG. Most were generated from genomic DNA isolated from mixed stage N2 animals.
364 Promoters include 4.8 kb (P*rig-3*), 0.9 kb (P*inx-1*), 5.3 kb (P*glr-1*), 2.9 kb (P*cex-1*), 0.86 kb (P*lgc-55B*),
365 3.1 kb (P*nmr-1*) genomic sequence. All promoters except P*nmr-1* and P*lgc-55B* used the genomic
366 sequence of the respective length starting immediately upstream of the predicted ATG start codon
367 of the respective genes. For P*nmr-1*, a 2 kb internal fragment which reduces the 5.1kb *nmr-1* re-
368 porter expression was removed (*Kawano et al., 2011*). Details on P*lgc-55B* can be found in *Gao*
369 *et al.* (*2015*).

370 Calcium imaging
371 For AIY calcium imaging, *aeaIs003* was generated by integrating *olaEx1621* [P*mod-1::GCaMP6s*; P*ttx-*
372 *3::RFP*; P*unc-122::mCherry*]). The integrant was outcrossed against N2 for 4 times to generate strain
373 ADS003, and crossed into *lite-1* to generate QW1410. As in previous studies, temperature-evoked
374 AIY activity was reliably recorded from neurites as opposed to the soma (*Clark et al., 2006*; *Biron*
375 *et al., 2006*).

376 For AFD calcium imaging, *aeaIs004* was generated by integrating an existing Ex line [P*gcy-8::GCaMP6s;*
377 *Pgcy-8::RFP; Punc-122::mCherry*]. The integrant was outcrossed against N2 for 4 times to generate
378 strain ADS004.

379 For premotor interneuron and motor neuron calcium imaging, pJH3338 was constructed for
380 calcium imaging for premotor interneurons and head motor neurons. The GCaMP6s reporter was
381 optimized for *C. elegans* and contained three *C. elegans* introns (*Lim et al., 2016*; *Chen et al., 2013*).
382 GCaMP6s was fused with codon-optimized mCherry (wCherry) at the C-terminus to facilitate ra-
383 tiometric measurement via simultaneous imaging of GFP and RFP. The reporter expression was

384 driven by P*glr-1* as described above. This construct was co-injected with lin-15(+) marker to *lin-*
385 *15(n765)* animals to generate extrachromosomal transgenic array *hpEx3550*, and subsequently in-
386 tegrated to generate *hpIs471*. The integrated array was outcrossed against N2 wild-type 4 times to
387 generate ZM8558. For simultaneous AIY and premoter/interneuron imaging, *hpIs471* was crossed
388 with *aeaIs003* to generate ADS027.

Neuron ablation

390 pJH2829, pJH3311, pJH2931, pJH2890, and pJH2827 were constructed for LED-based neuronal abla-
391 tion for RIM, AIB, AVA (plus other neurons), AVB (plus other neurons), and AVA/AVE/AVD/RIM/PVC
392 (plus other neurons), respectively. miniSOG fused with an outer mitochondrial membrane tag
393 TOMM20 (tomm20-miniSOG or mito-miniSOG) (*Qi et al., 2012*; *Shu et al., 2011*). An inter-cistronic
394 sequence splice leader (SL2) was inserted between the coding sequence of tomm20-miniSOG and
395 codon-optimized mCherry (wCherry; a gift of A. Desai, UCSD) to visualize neurons that express
396 miniSOG, and to examine the efficacy of ablation. SL2 sequence was PCR amplified off the splice
397 leader sequence (SL2) between *gpd-2* and *gpd-3*. These constructs were co-injected with the lin-
398 15(+) marker in *lin-15(n765)* animals to generate extrachromosomal arrays *hpEx2997*, *hpEx3464*,
399 *hpEx3072*, *hpEx3064*, and *hpEx2940*, respectively. With the exception of *hpEx3072*, other arrays
400 were integrated to generate *hpIs327*, *hpIs465*, *hpIs331*, and *hpIs321*. All integrated transgenic ar-
401 rays were outcrossed 4 times against N2, except *hpIs327*, which was outcrossed 7 times against
402 N2, before being used for behavioral analyses or to be combined with AIY calcium imaging analy-
403 ses, or, behavioral analyses.

AIY imaging upon neuronal ablation

405 *aeaIs003* was crossed with *hpIs327*, *hpIs321*, *hpEx3072*, *hpIs331*, and *hpIs465*, respectively, to gener-
406 ate ADS010, ADS014, ADS026, ADS036 and ADS046. They were used for AIY calcium imaging upon
407 ablation of RIM, premotor interneurons (with a few other neurons), and AIB, respectively.

AIY calcium imaging upon genetic manipulation of synaptic transmission and optogenetic stimulation

410 For AIY imaging in genetic synaptic transmission mutants, QW1408, QW1409, QW1411, QW1175,
411 and QW1415 were generated by crossing *aeaIs003* into the corresponding mutant backgrounds
412 listed in Supplemental Table 1.

413 For AIY imaging upon cell-type specific manipulation of synaptic transmission, *aeaIs003* was
414 crossed with *yxIs25*, *xuEx1414*, and *kyEx4962* to generate ADS043, ADS042, and ADS013, respec-
415 tively (*Li et al., 2014*; *Zhang et al., 2005*; *Gordus et al., 2015*).

416 Chrimson (*Klapoetke et al., 2014*) was codon-optimized and fused at C-terminus with wCherry
417 as described (*Lim et al., 2016*). Chrimson expression was driven by P*lgc-55B* and P*rig-3* to gener-
418 ate *pHR2* and *pHR6*. These constructs were co-injected with P*ges-1::GFP* into QW1410 to generate
419 *aeaEx003* (ADS29) and *aeaEx005* (ADS31), for AIY imaging upon optogenetic stimulation of AVB and
420 AVA, respectively.

421 *aeaEx003* and *aeaEx005* were then crossed into *hpIs327;aeaIs003;lite-1* to generate ADS033 and
422 ADS035 for AIY calcium imaging in RIM ablated animals, upon AVB and AVA stimulation, respec-
423 tively.

Behavioral assays

Positive thermotaxis assay

426 L4 animals were cultivated at 25°C the night before the assay. On the day of the experiment, the
427 behavioral arena was allowed to equilibrate until a stable linear thermal gradient spanning 19°C
428 to 23°C was established. Before each assay session, a thin layer of NGM agar sized 20 cm on each
429 side was placed on the arena and allowed to equilibrate to the temperature of the arena. Twenty
430 young adults were collected from their cultivation plates and briefly washed in NGM buffer before

they were transferred onto the thin agar. These animals were allowed to explore the assay environment for 5 minutes before behavioral recording starts. Afterwards, a CMOS camera positioned above the arena recorded continuously every 500 milliseconds for 20 minutes. Animal trajectories were extracted from the raw behavioral recordings using custom-written LABVIEW software. Subsequent analyses were performed in MATLAB.

Spontaneous locomotion assay

Animals were cultivated and prepared for behavioral assay in identical manners as for the positive thermotaxis assay. The same behavioral arena, equilibrate to room temperature (22°C), was used to assay spontaneous locomotion. Behavioral recordings were conducted the same way as in the positive thermotaxis assay. Subsequent analyses were performed using the same LABVIEW software as above and subsequently in MATLAB.

Calculation of thermotactic bias

For each animal, the instantaneous velocity (v) and speed ($|v|$) were calculated from the animal's centroid positions. The velocity vector was then projected onto direction of the thermal gradient, which in this case was parallel to the negative direction of the x-axis of the behavior arena. The thermotactic bias as the ratio between the velocity projection along the thermal gradient and the instantaneous speed of the animal:

$$\text{thermotactic bias} = \frac{-v_x}{|v|}$$

Calcium imaging in semi-constrained animals

Sample preparation and imaging setup

L4 larval animals expressing cytosolic GCaMP6s::wCherry were cultivated at 25°C the night before the imaging experiment. Immediately before the imaging session, animals were transferred to a microscope slide with a 5% agarose pad (2 mm thick). A small drop of NGM buffer was added to the agarose pad and a # 1 coverslip was lowered onto the pad. This preparation allowed the animal enough mobility to execute head and (partial) body oscillations characteristic of forward runs and reversals. Under this preparation, the animal exhibits slow, local displacements, but cannot fully leave the field of view. Calcium imaging was performed on an upright spinning disc confocal microscope (Nikon Eclipse LV100 and Yokogawa CSU22) and iXon3 DU-897 EMCCD camera (Andor). High resolution images were collected through a 40x, 0.95 NA Nikon Plan Apo lambda objective. 3D volumetric stacks were acquired in both the green (GCaMP6s) and red (wCherry) channels with an exposure of 30 ms at approximately 1.2 volumes per second.

Control of thermal stimulation

Animals were imaged on a custom-built temperature control stage where a PID controller and H-bridge amplifier (Accuthermo) drove a thermoelectric cooler (TEC) (Newark) that pumped heat into and out of a thin copper plate with a liquid-cooled water block (Swiftech) acting as a thermal reservoir. A type-T thermocouple microprobe (Physitemp) was placed on the copper plate underneath a thin steel tab. A custom written Labview program was used to specify the desired temperature waveform.

Extraction of calcium transient levels

To extract fluorescence intensities for individual neurons, we identified connected regions above a predefined intensity threshold and registered these regions of interest (ROI) across a movie based on spatial proximity across frames. For each ROI, we computed mean intensity of the top 30 pixels in both the green (GCaMP6s) and the red (wCherry) channel. The instantaneous activity of each neuron was computed using the following equation:

$$\Delta R(t)/R_0 = (R(t) - R_0)/R_0$$

475 R is the ratio between the mean intensity value in the green channel and that of the red channel.

476 R_0 represents the lowest 1st percentile of $R(t)$ values in the time series .

Event-triggered changes (ETA) in neural activity

478 AIY activity was extracted from a defined window of time spanning the event interest (i.e. onset of
479 thermal stimuli, transition between the forward run and reversal states, onset and offset of AVA
480 activation). For analysis in **Figure 3D**, AVA ON and OFF states were defined by thresholding AVA
481 activity using the Otsu method, which was implemented in MATLAB using the multithresh function.
482 Data across multiple epochs of the same event were concatenated into matrices and presented
483 as heat maps throughout the paper. Average ETA profiles were computed by averaging data from
484 that precede or lag the event of interest by the same number of time points.

Duration of AIY activation

486 AIY activity data from each imaging session was fit using a Gaussian mixture models (see Statistical
487 Analysis for implementation details). The number of Gaussian components were determined by
488 iteratively fitting models with component number k=1,2,3,...,6 and assessing the quality of the fit
489 using the Bayesian Information Criterion (BIC). As k increases, the BIC value typically drops sharply
490 from k=2 to k=3 and varies little after that. For wild type data, models with k=3 consistently capture
491 the baseline AIY activities during reversals, the heightened activities during forward runs, and the
492 large transients that occur at the onset of the forward runs or in response to warming stimuli.
493 We thus defined the intersection point of the two Gaussian components with the lowest and the
494 second lowest mean as the threshold above AIY is considered to be in the activated state. We then
495 use this threshold value to binarize the AIY activity time series and compute the duration of each
496 bout of AIY activation.

Optogenetic stimulation and simultaneous calcium imaging

498 Experimental animals expressing Chrimson were grown on NGM plates supplied with 5 μM all-
499 trans retinal (ATR) mixed with OP50 bacteria. Control animals of the same genotypes were grown
500 on NGM plates seeded with OP50 without ATR. The day before the experiment, L4 animals were
501 picked onto fresh plates (with ATR for the experimental groups and without ATR for the control
502 groups). On the day of the experiment, young adult animals were prepared for imaging in the
503 semi-constrained preparation as described above. During imaging, pulses of red light were deliv-
504 ered from a filtered white LED lamp. Pulse timing was controlled by MATLAB scripts. For calcium
505 imaging, animals were illuminated with only the blue laser (488 nm) to avoid strong activation of
506 Chrimson.

Neuron ablation

508 Transgenic animals expressing miniSOG were collected from late L1 to L2 stage onto a small NGM
509 plate (3.5 cm diameter). The plate was placed under a blue LED spotlight (Mightex, peak wavelength
510 617 nm) for 40 minutes. Following illumination, the animals were allowed to recover for overnight
511 at 15°C to examine the disappearance of cells. All ablation was performed using animals that
512 carried integrated miniSOG transgens, with the exception for AVA ablation. Ablation of AVA was
513 carried out in animals that carried an extrachromsomal array for *Prig-3-miniSOG-SL2-RFP*, which
514 was subjected to random loss during somatic division. Animals used for ablation were selected
515 for those that did not show expression (hence ablation) in a pharyngeal neuron that affects the
516 survival of ablated animals.

Statistical analysis

Statistical tests

519 The Wilcoxon rank-sum test were used in the following comparisons: 1) comparing calcium activity
520 upon the initiation of forward runs or reversals between wild type animals and various neuron-
521 ablation experiments, 2) comparing the probability of change in AIY activity upon the initiation of

522 forward run or reversals between wild type and AIY::TeTX animals, 3) comparing the thermotactic
523 bias between wild type and RIM ablated animals. To control for multiple comparison, p values were
524 adjusted using the Benjamini-Hochberg correction. 95% confidence intervals were determined by
525 bootstrapping.

526 Gaussian mixture model
527 Gaussian mixture models were fit to AIY activity distributions from each independent dataset using
528 the fitgmdist function in MATLAB. The initial cluster centers were generated through the k-means++
529 algorithm and the initial mixing proportions were set to uniform.

530 **Modeling of circuit activity and behavior**
531 Neural circuit model
532 We use a minimal model to capture the interaction between the key components of the thermo-
533 taxis circuit:

$$\text{Thermosensory neuron (AFD) - } V_0: \quad \tau_0 \frac{dV_0}{dt} = -g_{L0}\left(V_0 - V_{L0}\right) + I_{input}R \tag{1}$$

$$\text{Interneuron (AIY) - } V_1: \quad \tau_1 \frac{dV_1}{dt} = -g_{L1}\left(V_1 - V_{L1}\right) + F_{10}V_0 + F_{12}V_2 \tag{2}$$

$$\text{Motor command neurons - } V_2: \quad \tau_2 \frac{dV_2}{dt} = -g_{L2}\left(V_2 - V_{L2}\right) + F_{21}V_1 \tag{3}$$

534 where g_{L1}, g_{L2}, and g_{L3} are leak conductances and are non-negative. V_{L1}, V_{L2}, and V_{L3} are the resting
535 potentials. Synaptic interactions are modeled as linear or sigmoidal functions:

$$F_{10}\left(V_0\right) = w_0 V_0 \tag{4}$$

$$F_{12}\left(V_2\right) = w_{fb}\left(\frac{1}{1 + e^{-k_1 \times (V_2 - \beta_1)}}\right) \tag{5}$$

$$F_{21}\left(V_1\right) = w_{21}\left(\frac{\gamma_1}{1 + e^{-k_2 \times (V_1 - \beta_2)}}\right) - \left(\frac{\gamma_2}{1 + e^{-k_3 \times \left(V_1 - \beta_2'\right)}}\right) \tag{6}$$

536 where w_0, w_{fb}, and w_{21} are the network weights, and g_i, k_i, and β_i define the height, steepness, and
537 inflection point of sigmoidal functions. The two terms in F_{32} represent separate groups of premotor
538 interneurons that promote forward runs (e.g., AVB) or reversals (e.g., AVA). Equation 6 essentially
539 performs a max operation between the two terms to determine whether the motor output favors
540 forward runs ($F_{32} > 0$) or reversals ($F_{32} < 0$).
541   The above model is further simplified by setting AFD activity to its steady state value, $V_0(t) \cong$
542 $V_0 = V_{L0} + \frac{I_{input}R}{g_{L0}}$, which reduces the model to two dimensions:

$$\tau_1 \frac{dV_1}{dt} = -g_{L1}V_1 + \alpha I_{input} + F_{12}\left(V_2\right) + C_1 \tag{7}$$

$$\tau_2 \frac{dV_2}{dt} = -g_{L2}V_2 + +F_{21}\left(V_1\right) + C_2 \tag{8}$$

543 where $\alpha = \frac{w_0 R}{g_{L1}}$, $C_1 = g_{L1}V_{L1} + V_{L0}$, and $C_2 = g_{L2}V_{L2}$.
544   Based on dynamical systems theory (*Strogatz, 2015*), the above model has two distinct stable
545 states as long as their nullclines intersect at least three times, which can be achieved by a wide
546 range of parameter values. *Table 1* lists the parameter values that were used for network simula-
547 tions in *Figure 7B*. Note that w_{fb} is varied between -1, 0, and 1, corresponding to negative feedback,
548 no feedback, and positive feedback networks.

Table 1. Parameter values used in *Figure 7B*

Parameter	Value
τ_1	2/3
τ_2	2/3
g_{L1}	1
g_{L2}	1
w_0	1
w_{fb}	-1,0,or 1
w_{21}	1
k_1	15
k_2	5
k_3	5
β_1	0
β_2	1.5
β_2'	1.5
γ_1	1
γ_2	1
C_1	0.5
C_2	0

Simulation of thermotaxis behavior

We used the same network model described above to drive agent behavior. The locomotory state $M(t)$ of the animal is determined by the activity of the motor command neuron:

$$M(t) = 1, \text{ if } V_2 > 0 \rightarrow \text{agent executes forward run}$$
$$M(t) = 0, \text{ if } V_2 < 0 \rightarrow \text{agent executes reversal}$$

At the start of each forward run, the new heading direction is chosen randomly from a uniform distribution with range $[-180°,180°)$. During an ongoing forward run or reversal, the heading direction, $\theta(t)$, was kept constant. When a forward run ends and a reversal state starts, the heading direction changes by 180°:

$$\theta(t) = \begin{cases} (\cos\theta_0, \sin\theta_0) & t = 0 \\ \theta(t-dt) & M(t) = M(t-dt) \\ -\theta(t-dt) & M(t) = 1 \text{ and } M(t-dt) = -1 \\ \cos\theta_0, \sin\theta_0) & M(t) = -1 \text{ and } M(t-dt) = 1 \end{cases} \tag{9}$$

These simple behavioral rules allows us to specifically model the biased random walk component of thermotaxis, while leaving the RIM-independent klinotaxis component out of the analysis. All agents are simulated to move at constant speed (1 unit length per time step) on a two-dimensional linear thermal gradient. The gradient is set to lie along the x-axis: $T(x) = c_T x$, where x represents the x coordinate. Since AFD is known to sense temporal changes in temperature, the input current to AFD evoked by thermal stimuli is defined by $I_input(t) = c_T(x(t) - x(t - \Delta t))$ where $x(t)$ is the instantaneous x-position of the agent.

Each simulation is initialized by setting an starting position of (0,0), an initial heading angle drawn from the uniform distribution from $[-180°,180°)$, an initial network state of $(V_1(t_0) = 1, V_2(t_0) = 1)$, and with the animal in a forward run state. Upon numerical integration, simulated worms move autonomously in their environment for a predetermined duration (t_{max}).
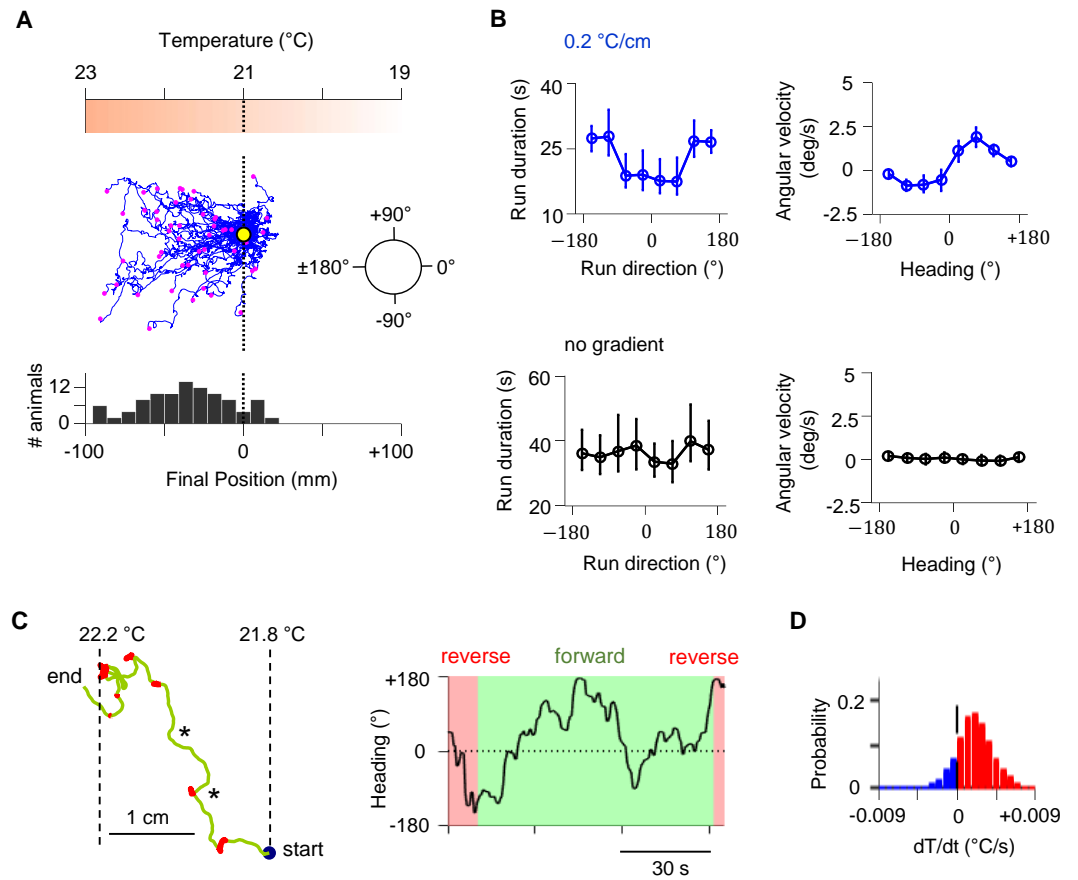
Figure 1. Sustained forward motor state despite temperature fluctuations during positive thermotaxis. A. Example trajectories of wild type *C. elegans* cultivated at 25°C migrating up a linear temperature gradient over 20 minutes. Top, schematics of the thermal gradient. Middle, trajectories of 49 animals during positive thermotaxis. The starting points of all trajectories are aligned (yellow dot) and the end points are marked by magenta dots. Bottom, a histogram of the final location of animals. **B.** Left column: Duration of forward runs as a function of their overall direction (vector pointing from the starting point to the end point of the run). Right column: Instantaneous velocity during forward runs as a function of the instantaneous heading angle. Top row: Data from animals exposed to spatial thermal gradients (top, N = 140). Bottom row: Data from animals under constant temperature surfaces (bottom, N = 73). **C.** Thermotaxis trajectory of a single animal during thermotaxis with alternating periods of forward movement and reversals (left), and the instantaneous heading angle over time during one extended period of forward movement within the trajectory (right). Asterisks denote periods where the heading direction pointed down the thermal gradient. **D.** Histogram of temporal changes in temperature (dT/dt) experienced by animals during forward runs that ended up pointing up the temperature gradient. Data from N=140 wild-type animals exposed to linear thermal gradient and N=73 wild-type animals exposed to constant temperature of 21 °C. Error bars are standard errors of the mean (s.e.m.).

Figure 1–Figure supplement 1. Distribution of thermal fluctuations experienced by *C. elegans* animals during positive chemotaxis.
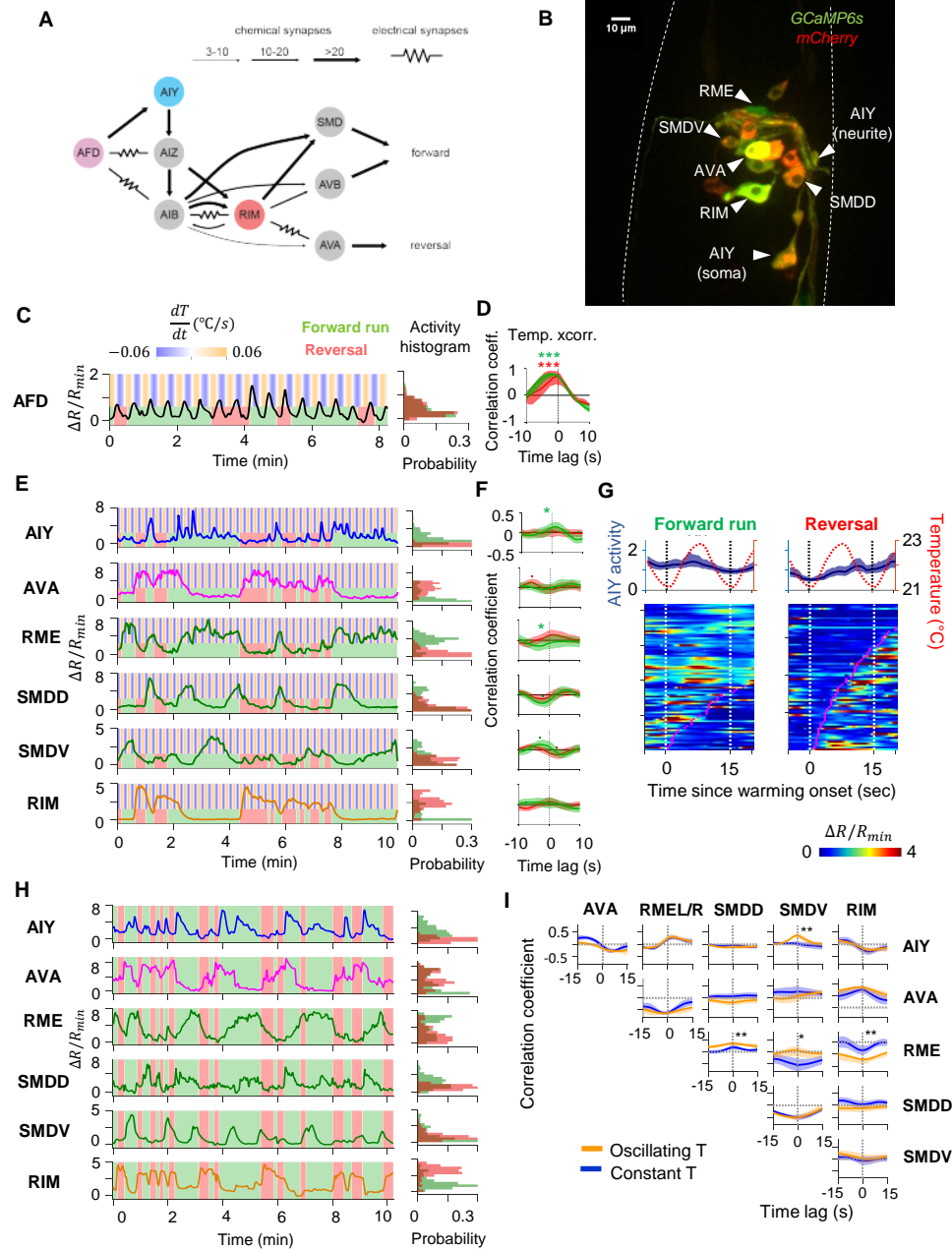
Figure 2. Characterization of circuit-level neural activity in the behaving animal with fluctuating or constant temperatures. A. Anatomical connections among neurons implicated in positive thermotaxis, locomotory control, or both. Connectivity is inferred from both the original *C. elegans* connectome (***White et al., 1986***) and a recent reconstruction of the connectome across the developmental time course (***Witvliet et al., 2020***) (see www.nemanode.org) **B.** Example maximum projection of a confocal z-stack taken from a transgenic animal expressing GCaMP6s and mCherry in neurons examined in this study. **C.** Example ratiometric calcium activity trace (left panel) and histogram (right panel) of the thermosensory neuron AFD in response to oscillating temperature. **D.** Average cross-correlation function between thermal stimuli and AFD activity during forward run (green) or reversal (red) states. N=5-wild type animals. **E.** Simultaneously measured calcium activity of interneurons and motor neurons involved in thermosensory processing and/or motor control. The activity traces (left) and activity histograms (middle) are from the same sample dataset. **F.** Average cross-correlation functions between the thermal stimuli and individual neurons shown in **E**, conditioned on the animal in forward run (green) or reversal (red) states. N=6 wild-type animals. Error bars are 95% CI of the mean. Wilcoxon rank-sum test was used to compare the peak mean cross-correlation values during forward runs (green) versus reversals (red). * p<0.05; ** p<0.01; *** p<0.001; no asterisk p>0.05. **G.** Thermal stimulus-triggered activity of the AIY interneuron during forward runs (left column) and reversals (right column) in wild-type animals (N=5). Individual stimulus epochs from the same neuron under the given motor state were concatenated into heat maps, with the average calcium activity trace shown on top. **H.** Simultaneous recording of the activity of interneurons and motor neurons under constant temperature. The histograms on the right are derived from the sample activity traces to the left. **I.** Pair-wise cross-correlation functions among neurons examined in **E** and **H** under oscillating (orange, N=6) or constant temperature (blue, N=7). Error bars are standard errors of the mean (s.e.m.). Wilcoxon rank-sum test was used to compare the peak mean cross-correlation values between data under oscillating temperature versus data under constant temperature. * p<0.05; ** p<0.01; *** p<0.001; no asterisk p>0.05.

Figure 2–Figure supplement 1. Behavior state annotation in free-moving and semi-constrained animals
Figure 2–Figure supplement 2. Thermal response of AIY under different locomotory states
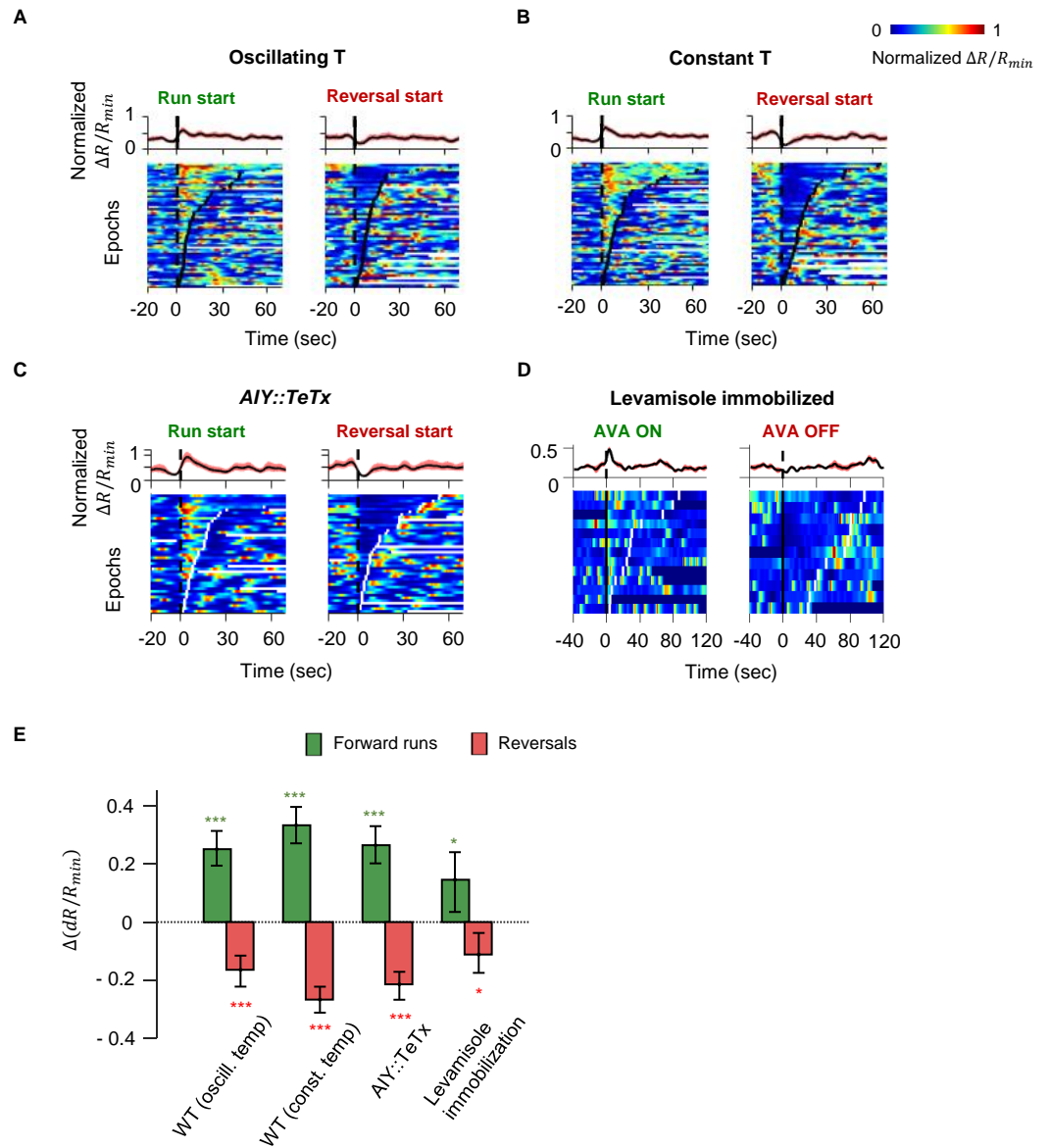
Figure 3. Motor-related activity in the AIY interneuron represents a corollary discharge signal.A-B.
Calcium activity of the AIY interneuron aligned to the onset of forward runs (left column) or reversals (right column) in animals exposed to oscillating temperature (**A**, N=6) or constant temperature (**B**, N=5). Each row of the heat plots represents AIY calcium activity during a single behavioral epoch. The curve on top of each panel represents activity dynamics averaged across individual epochs. Broken lines indicate the onset and offset of each behavior epochs. **C.** Calcium activity of the AIY interneuron aligned to the onset of forward runs or reversals in animals expressing tetanus toxin (TeTx) specifically in AIY (N=4). **D.** Calcium activity of AIY aligned to onset or offset of AVA activation in animals immobilized by the cholinergic agonist levamisole (N=4). The ON and OFF states of AVA activity are defined by binarizing AVA activity using the Otsu method. See **Methods and Materials** for details). **E.** Change in AIY activity before v.s. after the onset of forward runs (green) or reversals (red) for datasets shown in **A** and **B**. Wilcoxon Signed Rank Test was used to test if the change in AIY activity has a median significantly different from zero, * p<0.05; ** p<0.01; *** p<0.001; n.s. indicates non-significant.

Figure 3–Figure supplement 1. Quantification of persistent activity in AIY in wild type animals.
Figure 3–Figure supplement 2. Circuit-level neural activity in immobilized animals
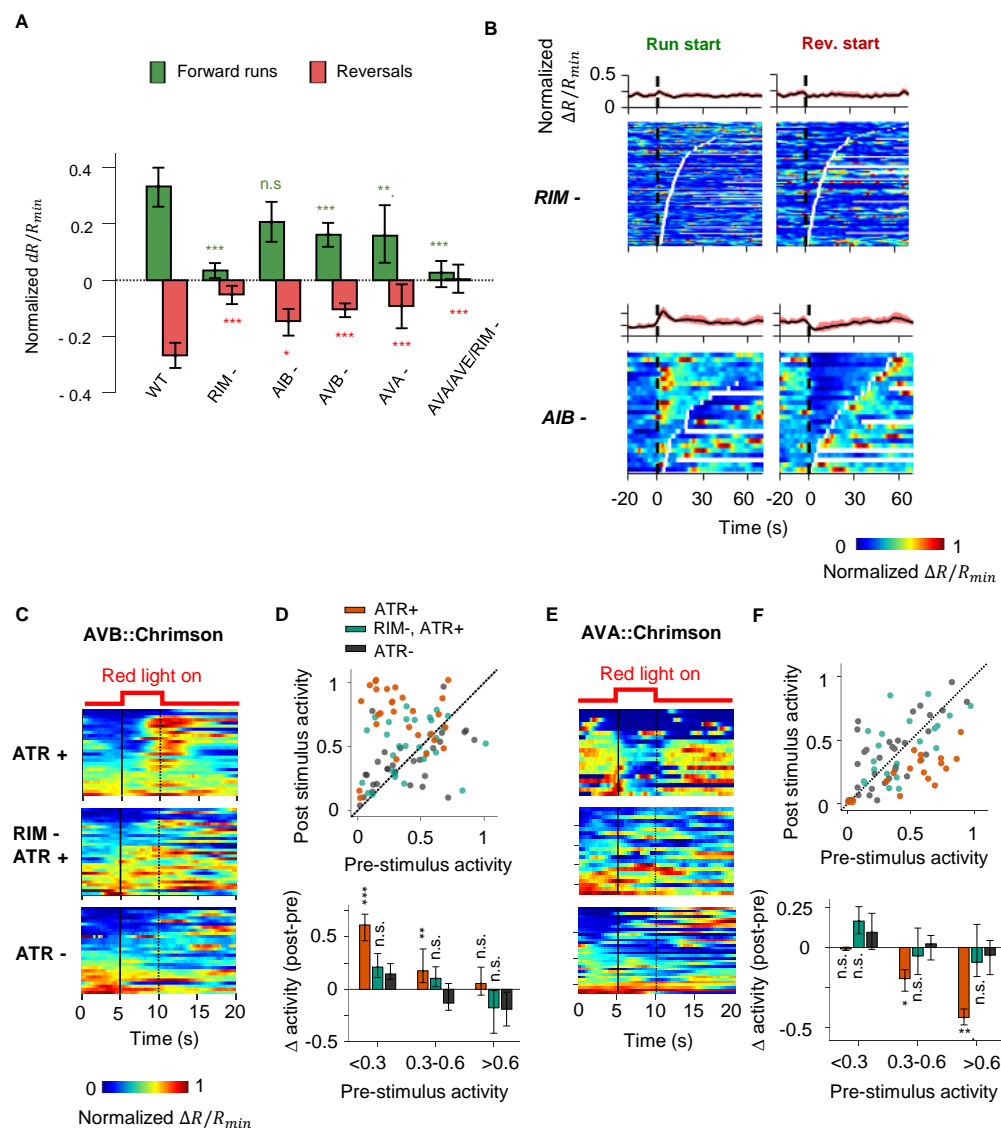
Figure 4. A corollary discharge pathway that requires the RIM interneuron couples AIY activity with the motor state.A. Change in AIY activity before v.s. after the onset of forward runs (green) or reversals (red) in animals where candidate neurons for relaying the CD signal have been ablated. Data are from RIM ablated animals (N=9); AIB ablated animals (N=3); AVB ablated animals (N=4); AVA ablated animals (N=4); and AVA/AVE/RIM (*nmr-1::miniSOG*) ablated animals (N=4). Error bars are 95% CI. Wilcoxon rank-sum test was used to test if the distributions of AIY activity before and after the onset of motor states have the same median: * p<0.05; ** p<0.01; *** p<0.001; no asterisk p>0.05. **B.** AIY activity aligned to the onset of forward runs (left column) or reversals (right column) in the animals where neurons RIM (upper panels, N = 9) or AIB (lower panels, N = 3) have been genetically ablated. **C.** AIY activity in response to optogenetic stimulation of the AVB pre-motor interneurons in wild-type animals grown on all-trans retinal (ATR) (top, N = 5), RIM ablated animals grown on ATR (N = 6), and wild-type animals grown without ATR (N = 3). **D.** Top: AIY activity 2.5 seconds before (pre-stimulus) versus 2.5 seconds at the end of the AVB opto-stimulation (post-stimulus) under experimental conditions shown in **D**. Bottom: Average change in AIY activity pre-and post-stimulation under experimental conditions shown **D**. Trials are sorted into three groups based on pre-stimulation AIY activity. Same datasets as in **C**. **E.** AIY activity in response to optogenetic stimulation of the AVA pre-motor interneurons in wild-type animals grown on all-trans retinal (ATR) (top, N=4), RIM ablated animals grown on ATR (middle, N=5), and wild-type animals grown without ATR (bottom, N=5). **F.** Top: AIY activity 2.5 seconds before (pre-stimulus) versus 2.5 seconds at the end of the AVA opto-stimulation (post-stimulus) under experimental conditions shown in **E**. Bottom: Average change in AIY activity pre- and post-stimulation under experimental conditions shown in **E**. Trials are sorted into three groups based on pre-stimulation AIY activity. Same datasets as in **E**. For **E** and **F**, error bars are 95% CI; Wilcoxon signed-rank test was used to test if the average post-stimulation change in AIY activity was significantly different from 0. * p<0.05; ** p<0.01; *** p<0.001; no asterisk p>0.05.

Figure 4–Figure supplement 1. AIY activity aligned to behavioral states in animals where candidate neurons for relaying the corollary discharge (CD) signal have been ablated

Figure 4–Figure supplement 2. AIY activity aligned to motor states in mutant and transgenic animals defective in various modes of chemical transmission
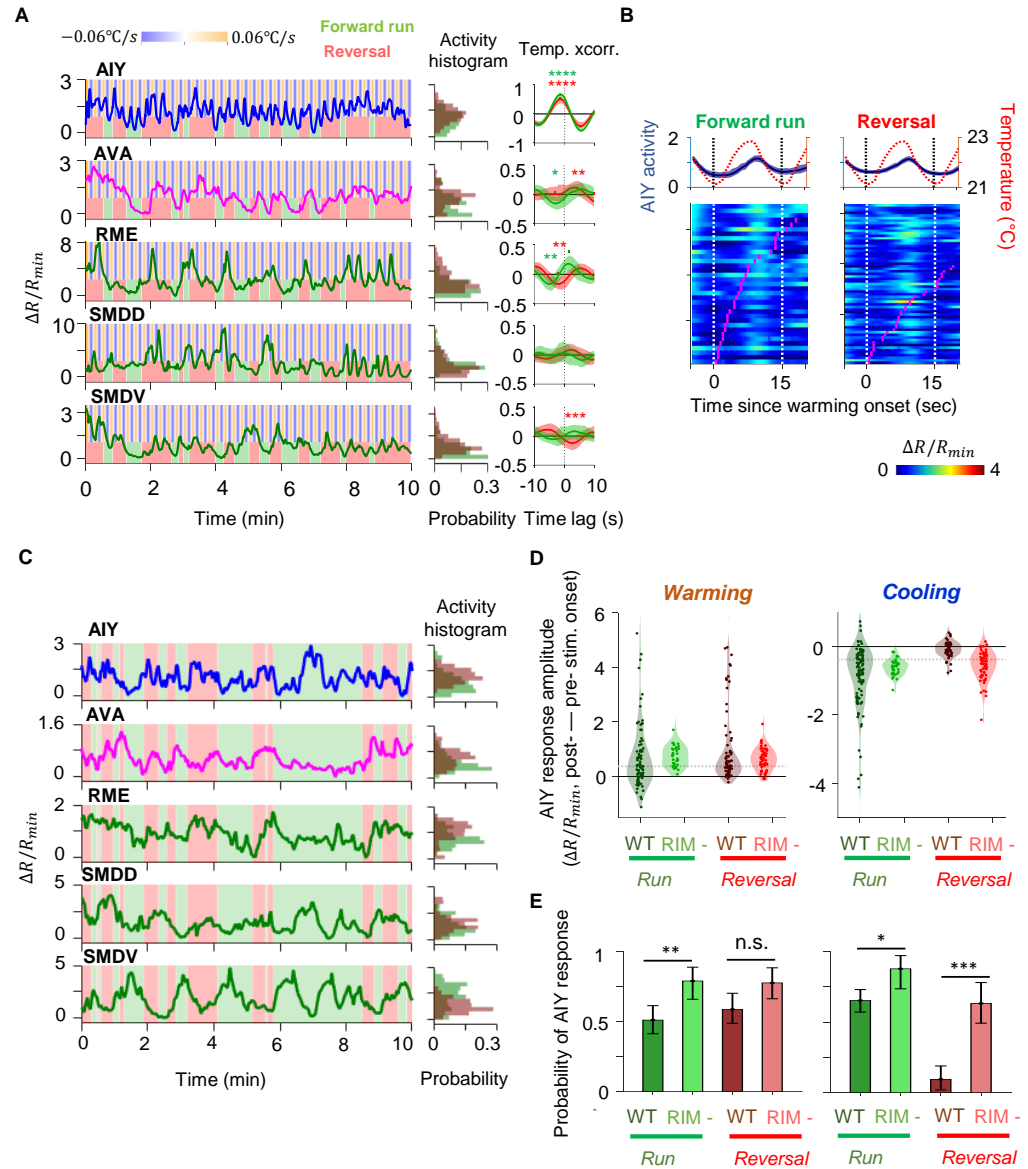
Figure 5. Characterization of circuit-level neural activity in behaving RIM-ablated animals under fluctuating or constant temperature. A. Simultaneously measured activity of AIY and neurons of the motor circuit in RIM-ablated animals under oscillating temperature. Middle panels show histograms of neuron activity during forward runs (green) or reversals (red) for the dataset to the left. Right panels show average cross-correlograms between neural activity and thermal stimuli during forward runs and reversals across RIM-ablated animals (N=3). Error bars are 95% CI of the mean. Wilcoxon rank-sum test was used to compare the peak mean cross-correlation values during forward runs (green) versus reversals (red). * p<0.05; ** p<0.01; *** p<0.001; no asterisk p>0.05. **B.** Thermal stimulus-triggered activity of the AIY interneuron during forward runs (left column) and reversals (right column) in RIM-ablated animals (N=3). Individual stimulus epochs from the same neuron under the given motor state were concatenated into heat maps, with the average activity trace shown on top. **C.** Simultaneously measured activity of AIY and neurons of the motor circuit in RIM-ablated animals under constant temperature (left). Right panels show histograms of neuron activity during forward runs (green) or reversals (red). **D.** Violin plots showing the distribution of changes in AIY activity in response to warming (left) or cooling (right) stimuli under forward run or reversal state in wild-type and RIM-ablated animals. Dotted black lines indicate threshold values used to calculate the response probability in **E**. **E.** Probability that the magnitude of change in AIY activity upon warming or cooling is above defined thresholds in wild-type or RIM-ablated animals. See **Methods and Materials** for details. For **D** and **E**, N=5 wild-type animals and N=3 RIM ablated animals. Error bars are 95% CI of the mean. Wilcoxon rank-sum test * p<0.05; ** p<0.01; *** p<0.001; n.s. indicates non-significant.

Figure 5–Figure supplement 1. Analysis of AIY activity in RIM-ablated animals

A

23℃   19℃

180
−180 — 0

Count

6
0

-100   -50   0   50   100
Final position (mm)

B

Thermotactic bias

0.4

0.2

0

     ***

WT   RIM -

C

— WT
— RIM -

Run duration (s)

40

25

10

****   ***

**** ****

−180   0   180
Average run direction (deg)

D

WT   Velocity   RIM -

-5   5

Cooling instances

-20   0   20   0   4
Time relative to
cooling offset (s)

Post-cooling velocity

Cooling instances

-20   0   20   0   4
Time relative to
cooling offset (s)

Post-cooling velocity

E

WT

Probability

0.2

0

RIM -

0.2

0

-2.5   0   2.5
Post-cooling velocity

F

Fraction of cooling
followed by run termination

0.6

0

****   ****   ****   n.s.

— WT
— RIM -

<7   7-15   15-30   >30
Duration of cooling epoch (s)

Figure 6. RIM ablation disrupts positive thermotaxis and leads to increased susceptibility to sensory fluctuations. A. Example trajectories of RIM ablated animals (N = 39) cultivated at 25 °C and exposed to the same thermal gradient as in *Figure 1A*. Top, schematic of the thermal gradient. Middle, trajectories of individual animals during positive thermotaxis. The starting points of all trajectories are aligned (yellow dot) and the end points are marked by magenta dots. Bottom, a histogram of the final location of the animals at the end of the 20-minute period. **B.** Average thermotactic bias of wild type (N=140) versus RIM ablated animals (N=102). **C.** Forward run duration as a function of forward run direction in RIM-ablated animals (blue) compared to the wild-type (gray). Error bars are s.e.m. Wilcoxon rank-sum test was used to compare the run duration of wild type versus RIM ablated animals. p<*0.05, **0.01, ***0.001, p>0.05 (non-significant) for panels without asterisk. **D.** Velocity profiles of wild-type (left) and RIM-ablated (right) animals aligned to the end of cooling epochs that occurred during forward runs. Heat maps are generated by concatenating velocity profiles from individual cooling epochs along the y-axis, and sorting by the average velocity within the first 2 seconds after the offset of cooling epochs (shown as line plot to the right). Black dotted lines divide instances in which forward runs continued past the offset of cooling epochs from instances where reversals ensued within the first 2 minutes of cooling offset. **E.** Histograms of post-cooling velocities in wild type (top) and RIM ablated animals (bottom). Analysis applied to same data set as in **D**. **F.** Fraction of cooling epochs that were followed by transition from forward runs to reversals as a function of the duration of cooling epochs (orange: wild type, gray: RIM ablated).

Figure 6–Figure supplement 1. RIM ablation results in higher likelihood of forward runs ending after a period of cooling
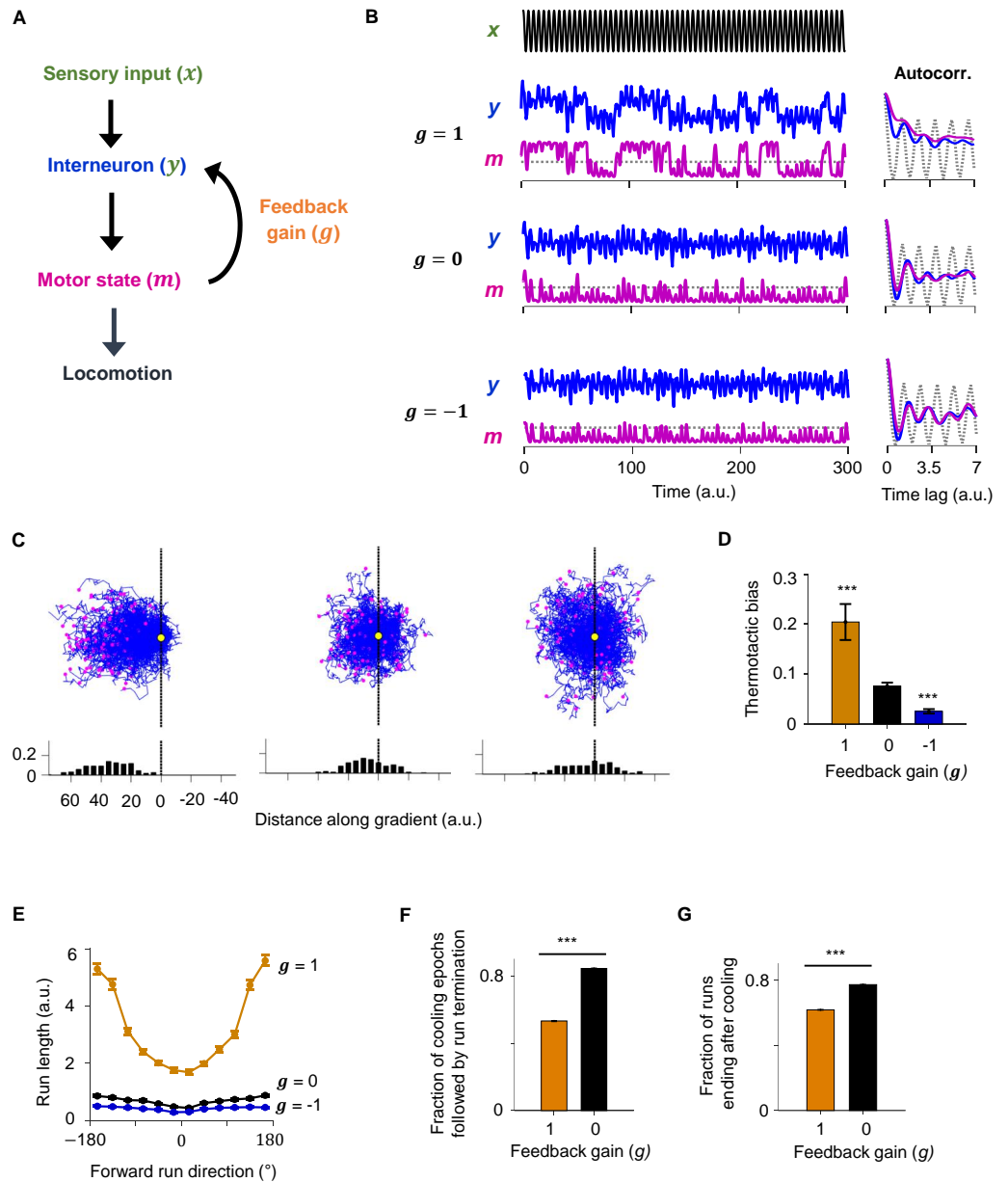
Figure 7. A reduced model explains the role of corollary discharge (CD) in sustaining forward locomotion during thermotaxis. A. Schematic of the circuit model. **B.** Dynamics of the model in response to an oscillating input stimulus. Top, temporal profile of the input signal. Middle, dynamics of the model with the feedback strength set to 1 (positive feedback), 0 (no feedback), or -1 (negative feedback). **C.** Simulated trajectories of navigational behavior on a 2-D arena with linear input gradient, with feedback strength set to 1 (left), 0 (middle), and -1 (right). **D.** Thermotactic biases for trajectories generated by models with feedback strength equaling 1 (positive feedback), 0 (no feedback), or -1 (negative feedback). **E.** Forward run duration as a function of forward run direction for the behavioral simulations in **D**. **F.** Fraction of cooling epochs that were followed by the termination of forward runs in simulations with the feedback gain set to 1 (blue) or 0 (black). **G.** Fraction of forward runs that ended after a period of cooling in simulations with the feedback gain set to 1 (blue) or 0 (black). Error bars are 95% CI. Wilcoxon rank-sum test * p<0.05; ** p<0.01; *** p<0.001.
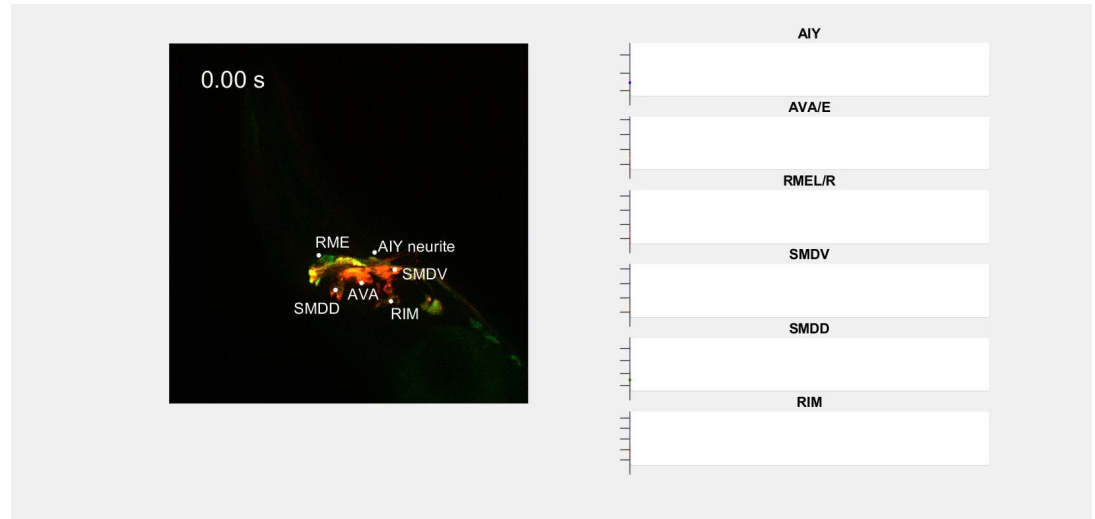
Video 1 Circuit-wide neural activity in semi-constrained wild-type animal exposed to oscillating temperature. Left: Calcium imaging of GCaMP6s (green) and wCherry (red) signals in head neurons involved in thermosen sory processing or locomotory control. Neuron names are listed next to the neur ite (AIY only) or soma (all other neurons) regions from which fluorescent signa ls are extracted. Video is sped up 5 times. Right: Ratiometric calcium activity traces extracted from the video to the left. Background colors indicate the os cillating thermal stimuli (blue-orange) and the forward run (green) and reversa l (red) states of the animal. Same data set as in *Figure 2E*.

```
File: WTosci.mp4
```
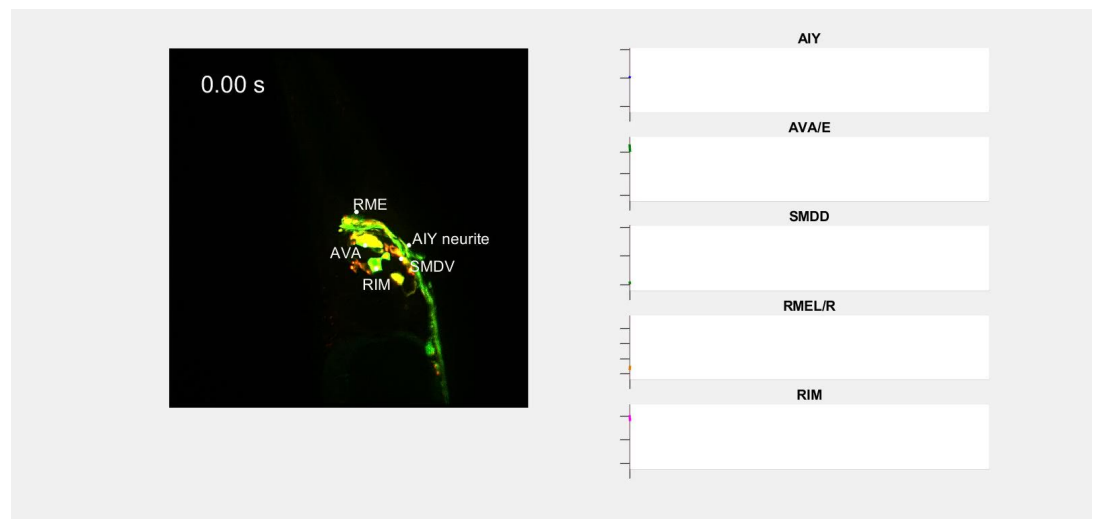

Video 2 Circuit-wide neural activity in semi-constrained wild-type animal exposed to constant temperature. Left: Calcium imaging of GCa MP6s (green) and wCherry (red) signals in head neurons involved in thermosensor y processing or locomotory control. Neuron names are listed next to the neurite (AIY only) or soma (all other neurons) regions from which fluorescent signals are extracted. Video is sped up 5 times. Right: Ratiometric calcium activity tr aces extracted from the video to the left. Background colors indicate the forwa rd run (green) and reversal (red) states of the animal. Same data set as in *Figure 2H*.

```
File: WTconst_T.mp4
```
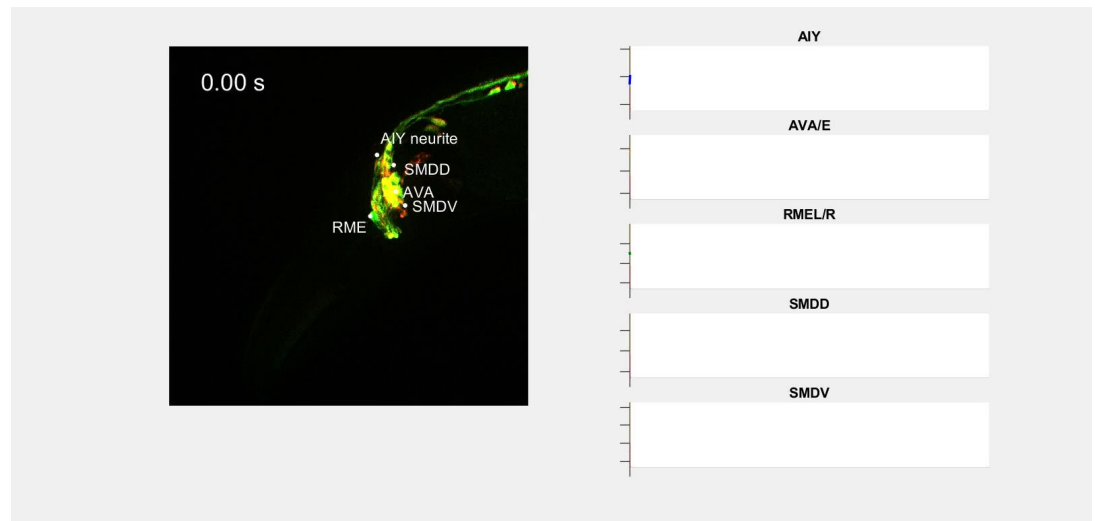
Video 3 Circuit-wide neural activity in semi-constrained RIM-ablated animal exposed to oscillating temperature. Left: Calcium imaging o f GCaMP6s (green) and wCherry (red) signals in head neurons involved in thermos ensory processing or locomotory control. Neuron names are listed next to the ne urite (AIY only) or soma (all other neurons) regions from which fluorescent sig nals are extracted. Video is sped up 5 times. Right: Ratiometric calcium activi ty traces extracted from the video to the left. Background colors indicate the oscillating thermal stimuli (blue-orange) and the forward run (green) and rever sal (red) states of the animal. Same data set as in *Figure 5A*.

File: RIMabl_osci_T.mp4

Acknowledgements

We thank Daniel Witvliet for insights on *C. elegans* connectomes and generating Figures 2B and 4A. We thank the laboratories of Yun Zhang, Daniel Colón-Ramos, Shawn Xu and Cori Bargmann for strains. This work was suppported by NIH P01 GM103770 (ADTS), NIH R01 NS082525-01A1 (ADTS, MZ, MJA), NIH R01 GM084491 (MJA), the Burroughs Wellcome (VV), and the CIHR foundation 154274 (MZ). We thank Steven Flavell and members of the Samuel, Alkema, and Zhen laboratories for constructive advice and help in completion of the study and manuscript preparation.

References

Aimon S, Katsuki T, Jia T, Grosenick L, Broxton M, Deisseroth K, Sejnowski TJ, Greenspan RJ. Fast near-whole-brain imaging in adult drosophila during responses to stimuli and behavior. PLoS Biology. 2019; 17(2):1–31.

Aksay E, Olasagasti I, Mensh BD, Baker R, Goldman MS, Tank DW. Functional dissection of circuitry in a neural integrator. Nature neuroscience. 2007; 10(4):494–504.

Alkema MJ, Hunter-Ensor M, Ringstad N, Horvitz HR. Tyramine functions independently of octopamine in the Caenorhabditis elegans nervous system. Neuron. 2005; 46(2):247–260. doi: 10.1016/j.neuron.2005.02.024.

Bidaye SS, Machacek C, Wu Y, Dickson BJ. Neuronal Control of Drosophila. Science. 2014; 344:97–101. doi: 10.1126/science.1249964.

Biron D, Shibuya M, Gabel C, Wasserman SM, Clark DA, Brown A, Sengupta P, Samuel ADT. A diacylglycerol kinase modulates long-term thermotactic behavioral plasticity in C. elegans. Nature Neuroscience. 2006; 9(12):1499–1505.

Chalasani SH, Chronis N, Tsunozaki M, Gray JM, Ramot D, Goodman MB, Bargmann CI. Dissecting a circuit for olfactory behaviour in Caenorhabditis elegans. Nature. 2008; 451:6540–6540. doi: 10.1038/nature06540.

Chalfie M, Sulston JE, White JG, Southgate E, Thomson JN, Brenner S. The neural circuit for touch sensitivity in Caenorhabditis elegans. Journal of Neuroscience. 1985; 5(4):956–964. doi: 10.1523/jneurosci.05-04-00956.1985.

Chen TW, Wardill TJ, Sun Y, Pulver SR, Renninger SL, Baohan A, Schreiter ER, Kerr RA, Orger MB, Jayaraman V, Looger LL, Svoboda K, Kim DS. Ultrasensitive fluorescent proteins for imaging neuronal activity. Nature. 2013; 499(7458):295–300. doi: 10.1038/nature12354.

Clark DA, Biron D, Sengupta P, Samuel ADT, Clark, Biron D, Sengupta P, Samuel ADT. The AFD sensory neurons encode multiple functions underlying thermotactic behavior in Caenorhabditis elegans. Journal of Neuroscience. 2006; 26(28):7444–7451. doi: 10.1523/jneurosci.1137-06.2006.

Clark DA, Clark DA, Gabel CV, Gabel CV, Gabel H, Gabel H, Samuel ADT. Temporal Activity Patterns in Thermosensory Neurons of Freely Moving Caenorhabditis elegans Encode Spatial Thermal Gradients. Journal of Neuroscience. 2007; 27(23):6083–6090. doi: 10.1523/JNEUROSCI.1032-07.2007.

Crapse TB, Sommer MA. Corollary discharge across the animal kingdom. Nature Reviews Neuroscience. 2008; 9(8):587–600. doi: 10.1038/nrn2457.

Ferrée TC, Ferrée F, Lockery SR. Computational Rules for Chemotaxis in the Nematode C. elegans. Journal of Computational Neuroscience. 1999; 6:263–277.

Fontanini A, Katz DB. Behavioral states, network states, and sensory response variability. Journal of Neurophysiology. 2008; 100(3):1160–1168. doi: 10.1152/jn.90592.2008.

Fu Y, Tucciarone JM, Espinosa JS, Sheng N, Darcy DP, Nicoll RA, Huang ZJ, Stryker MP. A cortical circuit for gain control by behavioral state. Cell. 2014; 156(6):1139–1152. doi: 10.1016/j.cell.2014.01.050.

Gao S, Guan SA, Fouad AD, Meng J, Kawano T, Huang YC, Li Y, Alcaire S, Hung W, Lu Y, Qi YB, Jin Y, Alkema M, Fang-Yen C, Zhen M. Excitatory motor neurons are local oscillators for backward locomotion. eLife. 2018; 7:1–32.

Gao S, Xie L, Kawano T, Po MD, Guan S, Zhen M. The NCA sodium leak channel is required for persistent motor circuit activity that sustains locomotion. Nature Communications. 2015; 6:1–10. doi: 10.1038/ncomms7323.

Gordus A, Pokala N, Levy S, Flavell SW, Bargmann CI. Feedback from network states generates variability in a probabilistic olfactory circuit. Cell. 2015; 161(2):215–227.

Gray JM, Hill JJ, Bargmann CI. A circuit for navigation in Caenorhabditis elegans. Proceedings of the National Academy of Sciences of the United States of America. 2005; 102(9):3184–3191. doi: 10.1073/pnas.0409009101.

Hawk JD, Calvo AC, Liu P, Almoril-Porras A, Aljobeh A, Torruella-Suárez ML, Ren I, Cook N, Greenwood J, Luo L, Wang ZWW, Samuel ADT, Colón-Ramos DA. Integration of Plasticity Mechanisms within a Single Sensory Neuron of C. elegans Actuates a Memory. Neuron. 2018; 97(2):356–367.e4. doi: 10.1016/j.neuron.2017.12.027.

Hedgecock EM, Russell RL. Normal and mutant thermotaxis in the nematode Caenorhabditis elegans. Proceedings of the National Academy of Sciences of the United States of America. 1975; 72(10):4061–4065. doi: 10.1073/pnas.72.10.4061.

Hendricks M. Compartmentalized calcium dynamics in a C. elegans interneuron encode head movement. Nature. 2012; 487(7405):99–103. doi: 10.1038/nature11081.

Herberholz J, Antonsen BL, Edwards DH. A lateral excitatory network in the escape circuit of crayfish. The Journal of Neuroscience. 2002; 22(20):9078–9085.

Hobert O, Mori I, Yamashita Y, Honda H, Ohshima Y, Liu Y, Ruvkun G. Regulation of interneuron function in the C. elegans thermoregulatory pathway by the ttx-3 LIM homeobox gene. Neuron. 1997; 19(2):345–357. doi: 10.1016/S0896-6273(00)80944-7.

Holst E, Mittelstaedt H. The principle of reafference: Interactions between the central nervous system and the peripheral organs. Die Naturwissenschften. 1950; 37:464–476.

Hoopfer ED, Jung Y, Inagaki HK, Rubin GM, Anderson DJ. P1 interneurons promote a persistent internal state that enhances inter-male aggression in Drosophila. eLife. 2015; 4:1–27. doi: 10.7554/eLife.11346.

Ikeda M, Nakano S, Giles AC, Xu L, Costa WS, Gottschalk A, Mori I. Context-dependent operation of neural circuits underlies a navigation behavior in Caenorhabditis elegans. Proceedings of the National Academy of Sciences of the United States of America. 2020; 117(11):6178–6188.

Inagaki HK, Fontolan L, Romani S, Svoboda K. Discrete attractor dynamics underlies persistent activity in the frontal cortex. Nature. 2019; 566(7743):212–217. doi: 10.1038/s41586-019-0919-7.

Ino Y, Yoshida K. Parallel use of two behavioral mechanisms for chemotaxis in Caenorhabditis elegans. Journal of Neuroscience. 2009; 29(17):5370–5380. doi: 10.1523/JNEUROSCI.3633-08.2009.

Kaplan HS, Nichols ALA, Zimmer M. Sensorimotor integration in Caenorhabditis elegans: A reappraisal towards dynamic and distributed computations. Philosophical Transactions of the Royal Society B: Biological Sciences. 2018; 373(1758).

Kaplan HS, Salazar Thula O, Khoss N, Zimmer M. Nested Neuronal Dynamics Orchestrate a Behavioral Hierarchy across Timescales. Neuron. 2020; 105(3):562–576.e9.

Kato S, Kaplan HS, Schrödel T, Skora S, Lindsay TH, Yemini E, Lockery S, Zimmer M. Global Brain Dynamics Embed the Motor Command Sequence of Caenorhabditis elegans. Cell. 2015; 163(3):656–669.

Kawano T, Po MD, Gao S, Leung G, Ryu WS, Zhen M. An imbalancing act: Gap junctions reduce the backward motor circuit activity to bias C. elegans for forward locomotion. Neuron. 2011; 72(4):572–586.

Kennedy A, Kunwar PS, yun Li L, Stagkourakis S, Wagenaar DA, Anderson DJ. Stimulus-specific hypothalamic encoding of a persistent defensive state. Nature. 2020; 586(7831):730–734. doi: 10.1038/s41586-020-2728-4.

Kim AJ, Fitzgerald JK, Maimon G. Cellular evidence for efference copy in Drosophila visuomotor processing. Nature neuroscience. 2015; 18(9):1247–1255.

Klapoetke NC, Murata Y, Kim SS, Pulver SR, Birdsey-Benson A, Cho YK, Morimoto TK, Chuong AS, Carpenter EJ, Tian Z, Wang J, Xie Y, Yan Z, Zhang Y, Chow BY, Surek B, Melkonian M, Jayaraman V, Constantine-Paton M, Wong GKS, et al. Independent optical excitation of distinct neural populations. Nature Methods. 2014; 11(3):338–346.

Kocabas A, Shen CH, Guo ZV, Ramanathan S. Controlling interneuron activity in Caenorhabditis elegans to evoke chemotactic behaviour. Nature. 2012; 490(7419):273–277. doi: 10.1038/nature11431.

Lee SH, Dan Y. Neuromodulation of brain states. Neuron. 2012; 76(1):209–222.

Lee S, Kruglikov I, Huang ZJ, Fishell G, Rudy B. A disinhibitory circuit mediates motor integration in the somatosensory cortex. Nature Neuroscience. 2013; 16(11):1662–1670. doi: 10.1038/nn.3544.

Li WC, Soffe SR, Wolf E, Roberts A. Persistent responses to brief stimuli: feedback excitation among brainstem neurons. The Journal of Neuroscience. 2006; 26(15):4026–4035.

Li Z, Liu J, Zheng M, Xu XZS. Encoding of both analog- and digital-like behavioral outputs by one C. Elegans interneuron. Cell. 2014; 159(4):751–765. doi: 10.1016/j.cell.2014.09.056.

Lim MA, Chitturi J, Laskova V, Meng J, Findeis D, Wiekenberg A, Mulcahy B, Luo L, Li Y, Lu Y, Hung W, Qu Y, Ho CY, Holmyard D, Ji N, McWhirter R, Samuel ADT, Miller DM, Schnabel R, Calarco JA, et al. Neuroendocrine modulation sustains the C. elegans forward motor state. eLife. 2016; 5. doi: 10.7554/eLife.19887.

López-Cruz A, Sordillo A, Pokala N, Liu Q, McGrath PT, Bargmann CI. Parallel Multimodal Circuits Control an Innate Foraging Behavior. Neuron. 2019; 102(2):407–419.e8. doi: 10.1016/j.neuron.2019.01.053.

Luo L, Clark DA, Biron D, Mahadevan L, Samuel ADT. Sensorimotor control during isothermal tracking in Caenorhabditis elegans. The Journal of Experimental Biology. 2006; 209(3):4652–4662.

Luo L, Cook N, Venkatachalam V, Martinez-Velazquez LA, Zhang X, Calvo AC, Hawk J, MacInnis BL, Frank M, Ng JHR, Klein M, Gershow M, Hammarlund M, Goodman MB, Colon-Ramos DA, Zhang Y, Samuel ADT, Colón-Ramos DA, Zhang Y, Samuel ADT, et al. Bidirectional thermotaxis in Caenorhabditis elegans is mediated by distinct sensorimotor strategies driven by the AFD thermosensory neurons. Proceedings of the National Academy of Sciences. 2014; 111(7):2776–2781. doi: 10.1073/pnas.1315205111.

Luo L, Wen Q, Ren J, Hendricks M, Gershow M, Qin Y, Greenwood J, Soucy ER, Klein M, Smith-Parker HK, Calvo AC, Colón-Ramos DA, Samuel ADT, Zhang Y, Colon-Ramos D, Samuel ADT, Zhang Y, Colón-Ramos DA, Samuel ADT, Zhang Y, et al. Dynamic encoding of perception, memory, and movement in a C. elegans chemotaxis circuit. Neuron. 2014; 82(5):1115–1128. doi: 10.1016/j.neuron.2014.05.010.

Major G, Tank D. Persistent neural activity: prevalence and mechanisms. Current opinion in neurobiology. 2004; 14(6):675–684.

Marques JC, Li M, Schaak D, Robson DN, Li JM. Internal state dynamics shape brainwide activity and foraging behaviour. Nature. 2020; 577(7789):239–243. doi: 10.1038/s41586-019-1858-z.

McCormick KE, Gaertner BE, Sottile M, Phillips PC, Lockery SR. Microfluidic Devices for Analysis of Spatial Orientation Behaviors in Semi-Restrained Caenorhabditis elegans. PloS one. 2011; 6(10):e25710.

McGinley MJ, Vinck M, Reimer J, Batista-Brito R, Zagha E, Cadwell CR, Tolias AS, Cardin JA, McCormick DA. Waking State: Rapid Variations Modulate Neural and Behavioral Responses. Neuron. 2015; 87(6):1143–1161. doi: 10.1016/j.neuron.2015.09.012.

Mori I, Ohshima Y. Neural regulation of thermotaxis in Caenorhabditis elegans. Nature. 1995; 376(6538):344–348. doi: 10.1038/376344a0.

Musall S, Kaufman MT, Juavinett AL, Gluf S, Churchland AK. Single-trial neural dynamics are dominated by richly varied movements. Nature Neuroscience. 2019; 22(10):1677–1686.

Narayan A, Laurent G, Sternberg PW. Transfer characteristics of a thermosensory synapse in Caenorhabditis elegans. Proceedings of the National Academy of Sciences of the United States of America. 2011; 108(23):9667–9672. doi: 10.1073/pnas.1106617108.

Nguyen JP, Shipley FB, Linder AN, Plummer GS, Liu M, Setru SU, Shaevitz JW, Leifer AM. Whole-brain calcium imaging with cellular resolution in freely behaving Caenorhabditis elegans. Proceedings of the National Academy of Sciences of the United States of America. 2016 jan; 113(8):E1074–E1081. doi: 10.1073/pnas.1507110112.

Ouellette MH, Desrochers MJ, Gheta I, Ramos R, Hendricks M. A Gate-and-Switch Model for Head Orientation Behaviors in Caenorhabditis elegans. Eneuro. 2018; 5(6):e0121–18.2018. doi: 10.1523/eneuro.0121-18.2018.

Petreanu L, Mao T, Sternson SM, Svoboda K. The subcellular organization of neocortical excitatory connections. Nature. 2009; 457(7233):1142–1145. doi: 10.1038/nature07709.

Pfister R, Schwarz K, Janczyk M, Dale R, Freeman J. Good things peak in pairs: a note on the bimodality coefficient. Frontiers in Psychology. 2013; 4:700. doi: 10.3389/fpsyg.2013.00700.

Pierce-Shimomura JT, Morse TM, Lockery SR, Lockery SR. The fundamental role of pirouettes in Caenorhabditis elegans chemotaxis. The Journal of Neuroscience. 1999; 19(21):9557–9569.

Pirri JK, McPherson AD, Donnelly JL, Francis MM, Alkema MJ. A Tyramine-Gated Chloride Channel Coordinates Distinct Motor Programs of a Caenorhabditis elegans Escape Response. Neuron. 2009; 62(4):526–538.

Poulet JFA, Hedwig B. A corollary discharge maintains auditory sensitivity during sound production. Nature. 2002; 418(6900):872–876. doi: 10.1038/nature00919.

Qi YB, Garren EJ, Shu X, Tsien RY, Jin Y. Photo-inducible cell ablation in Caenorhabditis elegans using the genetically encoded singlet oxygen generating protein miniSOG. Proceedings of the National Academy of Sciences of the United States of America. 2012; 109(19):7499–7504.

Requarth T, Sawtell NB. Plastic Corollary Discharge Predicts Sensory Consequences of Movements in a Cerebellum-Like Circuit. Neuron. 2014; 82(4):896–907. doi: 10.1016/j.neuron.2014.03.025.

Ryu WS, Samuel ADT. Thermotaxis in Caenorhabditis elegans analyzed by measuring responses to defined Thermal stimuli. The Journal of Neuroscience. 2002; 22(13):5727–5733.

Salkoff DB, Zagha E, McCarthy E, McCormick DA. Movement and Performance Explain Widespread Cortical Activity in a Visual Detection Task. Cerebral Cortex. 2020; 30(1):421–437.

Schneider DM, Nelson A, Mooney R. A synaptic and circuit basis for corollary discharge in the auditory cortex. Nature. 2014; 513(7517):189–194. doi: 10.1038/nature13724.

Seelig JD, Jayaraman V. Neural dynamics for landmark orientation and angular path integration. Nature. 2015; 521(7551):186–191. doi: 10.1038/nature14446.

Serrano-Saiz E, Poole RJ, Felton T, Zhang F, De La Cruz ED, Hobert O. XModular control of glutamatergic neuronal identity in C. elegans by distinct homeodomain proteins. Cell. 2013; 155(3):659. doi: 10.1016/j.cell.2013.09.052.

Seung HS. How the brain keeps the eyes still. Proceedings of the National Academy of Sciences. 1996; 93(23):13339–13344.

Shen Y, Wen Q, Liu H, Zhong C, Qin Y, Harris G, Kawano T, Wu M, Xu T, Samuel ADT, Zhang Y. An extrasynaptic GABAergic signal modulates a pattern of forward movement in Caenorhabditis elegans. eLife. 2016; 5:e14197. doi: 10.7554/eLife.14197.

Shu X, Lev-Ram V, Deerinck TJ, Qi Y, Ramko EB, Davidson MW, Jin Y, Ellisman MH, Tsien RY. A Genetically Encoded Tag for Correlated Light and Electron Microscopy of Intact Cells, Tissues, and Organisms. PLoS biology. 2011; 9(4):e1001041.

Sordillo A, Bargmann CI, Rockefeller T, Initiative CZ, City R. Behavioral control by depolarized and hyperpolarized states of an integrating neuron by. bioRxiv. 2021; p. 1–54. doi: 10.1101/2021.02.19.431690.

Sperry RW. Neural basis of the spontaneous optokinetic response produced by visual inversion. Journal of Comparative and Physiological Psychology. 1950; 43(6):482–489.

Stringer C, Pachitariu M, Steinmetz N, Reddy CB, Carandini M, Harris KD. Spontaneous behaviors drive multidimensional, brainwide activity. Science. 2019; 364(6437).

Strogatz SHSH. Nonlinear dynamics and chaos : with applications to physics, biology, chemistry, and engineering. Boulder, CO: Westview Press; 2015.

Taylor SR, Santpere G, Reilly M, Glenwinkel L, Poff A, McWhirter R, Xu C, Weinreb A, Basavaraju M, Cook SJ, Barrett A, Abrams A, Vidal B, Cros C, Rafi I, Sestan N, Hammarlund M, Hobert O, Miller DM. Expression profiling of the mature C. elegans nervous system by single-cell RNA-Sequencing. bioRxiv. 2019; doi: 10.1101/737577.

Tsalik EL, Hobert O. Functional mapping of neurons that control locomotory behavior in Caenorhabditis elegans. Journal of Neurobiology. 2003; 56(2):178–197. doi: 10.1002/neu.10245.

Venkatachalam V, Ji N, Wang X, Clark C, Mitchell JK, Klein M, Tabone CJ, Florman J, Ji H, Greenwood J, Chisholm AD, Srinivasan J, Alkema M, Zhen M, Samuel ADTT. Pan-neuronal imaging in roaming Caenorhabditis elegans. Proceedings of the National Academy of Sciences of the United States of America. 2016; 113(8):E1082—-8.

Wakabayashi T, Kitagawa I, Shingai R. Neurons regulating the duration of forward locomotion in Caenorhabditis elegans. Neuroscience Research. 2004; 50(1):103–111. doi: 10.1016/j.neures.2004.06.005.

Ward S. Chemotaxis by the nematode Caenorhabditis elegans: identification of attractants and analysis of the response by use of mutants. Proceedings of the National Academy of Sciences of the United States of America. 1973; 70(3):817–821. doi: 10.1073/pnas.70.3.817.

Whim MD, Niemann H, Kaczmarek LK. The secretion of classical and peptide cotransmitters from a single presynaptic neuron involves a synaptobrevin-like molecule. Journal of Neuroscience. 1997; 17(7):2338–2347. doi: 10.1523/jneurosci.17-07-02338.1997.

White JG, Southgate E, Thomson JN, Brenner S. The Structure of the Nervous System of the Nematode Caenorhabditis elegans. Philosophical Transactions of the Royal Society B: Biological Sciences. 1986; 314(1165):1–340. doi: 10.1098/rstb.1986.0056.

Witvliet D, Mulcahy B, Mitchell JK, Meirovitch Y, Berger DR, Wu Y, Liu Y, Koh WX, Parvathala R, Holmyard D, Schalek RL, Shavit N, Chisholm AD, Lichtman JW, Samuel ADT, Zhen M. Connectomes across development reveal principles of brain maturation in C. elegans. bioRxiv. 2020; .

Wurtz RH. Corollary discharge contributions to perceptual continuity across saccades. Annual Review of Vision Science. 2018; 4:215–237. doi: 10.1146/annurev-vision-102016-061207.

Yamaguchi S, Naoki H, Ikeda M, Tsukada Y, Nakano S, Mori I, Ishii S. Identification of animal behavioral strategies by inverse reinforcement learning. PLoS Computational Biology. 2018; 14(5):1–20. doi: 10.1371/journal.pcbi.1006122.

Yeon J, Kim J, Kim DY, Kim H, Kim J, Du EJ, Kang KJ, Lim HH, Moon D, Kim K. A sensory-motor neuron type mediates proprioceptive coordination of steering in C. elegans via two TRPC channels. PLoS Biology. 2018; 16(6):1–26.

Zagha E, Casale AE, Sachdev RNS, McGinley MJ, McCormick DA. Motor cortex feedback influences sensory processing by modulating network state. Neuron. 2013; 79(3):567–578. doi: 10.1016/j.neuron.2013.06.008.

Zhang Y, Lu H, Bargmann CI. Pathogenic bacteria induce aversive olfactory learning in Caenorhabditis elegans. Nature. 2005; 438(7065):179–184.

Appendix 1

Constructs and transgenic arrays

Calcium imaging			
Plasmid	**Injection Marker**	**Transgene**	**Strain**
pDACR1286[*Pmod-1::GCaMP6s*] (25ng/µl); pDACR63[*Pttx-3::mCherry*] (25ng/µl)	pDACR218[*Punc-122::dsRed*] (40ng/µl)	*aeaIs003(AIY) (integrated olaEx1621[a])*	ADS003
pDACR943[*Pgcy-8::GCaMP6s*] (30ng/µl);pDACR801 [*Pgcy-8::mCherry*] (5ng/µl)	pDACR20[*Punc122::GFP*] (20ng/µl)	*aeaIs004 (AFD) (integrated olaEx1527[b]*	ADS004
pJH3338[*Pglr-1-GCaMP6s::wCherry*]	pL15EK*lin-15AB genomic DNA* (20ng/µl)	*hpIs471 (premotor/ motor)*	ZM8558
Optogenetic stimulation			
pHR2[*Plgc-55B-Chrimson::wCherry*]	pL15EK[*lin-15AB genomic DNA*] (80ng/µl)	*aeaEx003 (AVB/others*	ADS029
pHR6[*Prig-3-Chrimson::wCherry*]	pL15EK[*lin-15AB genomic DNA*] (80ng/µl)	*aeaEx005 (AVA/others)*	ADS031
Cell ablation			
pJH2829[*Pcex-1- MiniSOG::SL2::wCherry*]	pL15EK[*lin-15AB genomic DNA*] (20ng/µl)	*hpIs327 (RIM)*	ZM7978
pJH3311[*Pinx-1- MiniSOG::SL2::wCherry*]	pL15EK[*lin-15AB genomic DNA*] (20ng/µl)	*hpIs465(AIB)*	ZM8484
pJH2931[*Prig-3- MiniSOG::SL2::wCherry*]	pL15EK[*lin-15AB genomic DNA*] (20ng/µl)	*hpEx3072 (AVA/others)*	ZM7198
pJH2890[*Plgc-55B- MiniSOG::SL2::wCherry*]	pL15EK[*lin-15AB genomic DNA*] (20ng/µl)	*hpIs331(AVB/others)*	ZM7297
pJH2890[*Pnmr-1-MiniSOG::SL2::wCherry*]	pL15EK[*lin-15AB genomic DNA*] (20ng/µl)	*hpIs321(AVA/E/D/RIM/PVC/others)*	ZM7054
Synaptic manipulation			
Pttx-3::TeTx::mCherry [c]		*yxIs25 (AIY)*	ZC1952
Ptdc-1::TeTx::mCherry [d]		*kyEx4962 (RIM/RIC)*	CX14993

[a]Gift of Daniel Colon-Ramos
[b]Gift of Daniel Colon-Ramos
[c]*Zhang et al.* (*2005*)
[d]*Gordus et al.* (*2015*)

Appendix 2

Strains

For thermotaxis and locomotion assays			
Strain	**Genotype**	**Purpose**	**Figure**
Bristol N2	wild-type	Wild-type behavior	*Figure 1A-D*
ZM7978	*hpIs327*	Behavior upon RIM ablation	*Figure 6*

Calcium imaging			
ADS003	*aeaIs003*	AIY imaging	*Figure 2E-I;3A,B*
ADS004	*aeaIs004*	AFD imaging	*Figure 2C,D*
ADS027	*aeaIs003; hpIs471*	Simultaneous imaging of AIY, AVA, RME, SMDD, SMDV and RIM	*Figure 2B,E*
ADS043	*aeaIs003; yxIs25*	AIY imaging, upon blockade of AIY chemical transmission	*Figure 3B*
ADS010	*aeaIs003; hpIs327*	AIY imaging, upon ablation of RIM	*Figure 4A,B;5A,C*
ADS014	*aeaIs003; hpIs321*	AIY imaging, upon ablation of RIM, AVA, AVE, AVD and PVC	*Figure 4A*
ADS026	*aeaIs003; hpEx3072*	AIY imaging upon ablation of AVA	*Figure 4A*
ADS036	*aeaIs003; hpIs331*	AIY imaging, upon ablation of AVB	*Figure 4A*
ADS046	*aeaIs003; hpIs465*	AIY imaging, upon ablation of AIB	*Figure 4A,B*
ADS029	*aeaEx003; aeaIs003; lite-1(ce314)*	AIY imaging upon optogenetic stimulation of AVB	*Figure 4C*
ADS031	*aeaEx005; aeaIs003; lite-1(ce314)*	AIY imaging upon optogenetic stimulation of AVA	*Figure 4E*
ADS033	*aeaEx005; aeaIs003; hpIs327; lite-1(ce314)*	AIY imaging, upon RIM ablation and AVA stimulation	*Figure 4E*
ADS035	*aeaEx003; aeaIs003; hpIs327; lite-1(ce314)*	AIY imaging, upon RIM ablation and AVB stimulation	*Figure 4C*
ADS013	*aeaIs003; kyEx4962*	AIY imaging, upon disruption of RIM/RIC chemical transmission	*Figure 4–Figure Supplement 2*
ADS006	*aeaIs003;tdc-1(n3419)*	AIY imaging in tyramine/octopamine synthesis mutant	*Figure 4–Figure Supplement 2*
QW1411	*aeaIs003; eat-4(ky5)*	AIY imaging in glutamate mutant	*Figure 4–Figure Supplement 2*
QW1175	*aeaIs003; unc-31(e928)*	AIY imaging in dense core vesicle release mutant	*Figure 4–Figure Supplement 2*
QW1408	*aeaIs003; cat-1(e1111)*	AIY imaging in biogenic amine transporter mutant	*Figure 4–Figure Supplement 2*

A

B

789

C

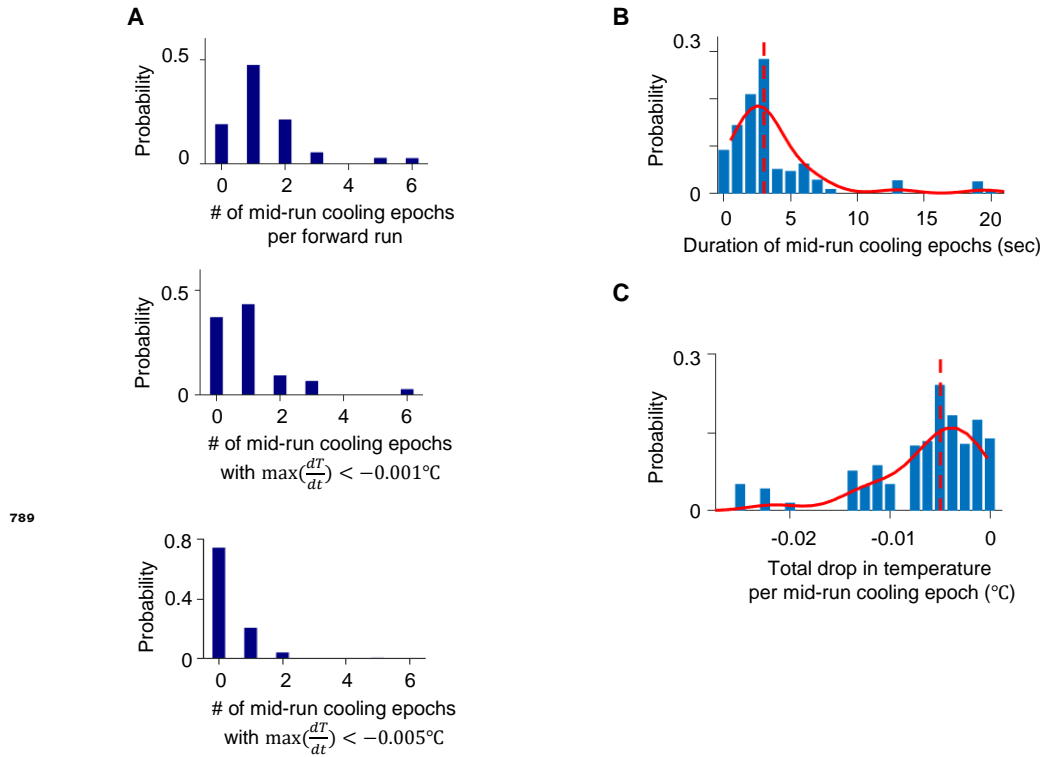**Figure 1–Figure supplement 1. Distribution of thermal fluctuations experienced by *C. elegans* animals during positive chemotaxis.A.** (Top) Distribution of the number of cooling epochs experienced during forward runs. Cooling epochs that occurred at the beginning or the end of forward runs were excluded. Same analysis carried out for cooling epochs where instantaneous temperature change was lower than -0.001 °C (middle) or -0.005 degree (bottom) throughout the epoch. **B.** Distribution of the duration of mid-run cooling epochs. **C.** Distribution of the total drop in temperature experienced during mid-run cooling epochs. Data from N=140 wild-type animals exposed to linear thermal gradients shown in **Figure 1A**
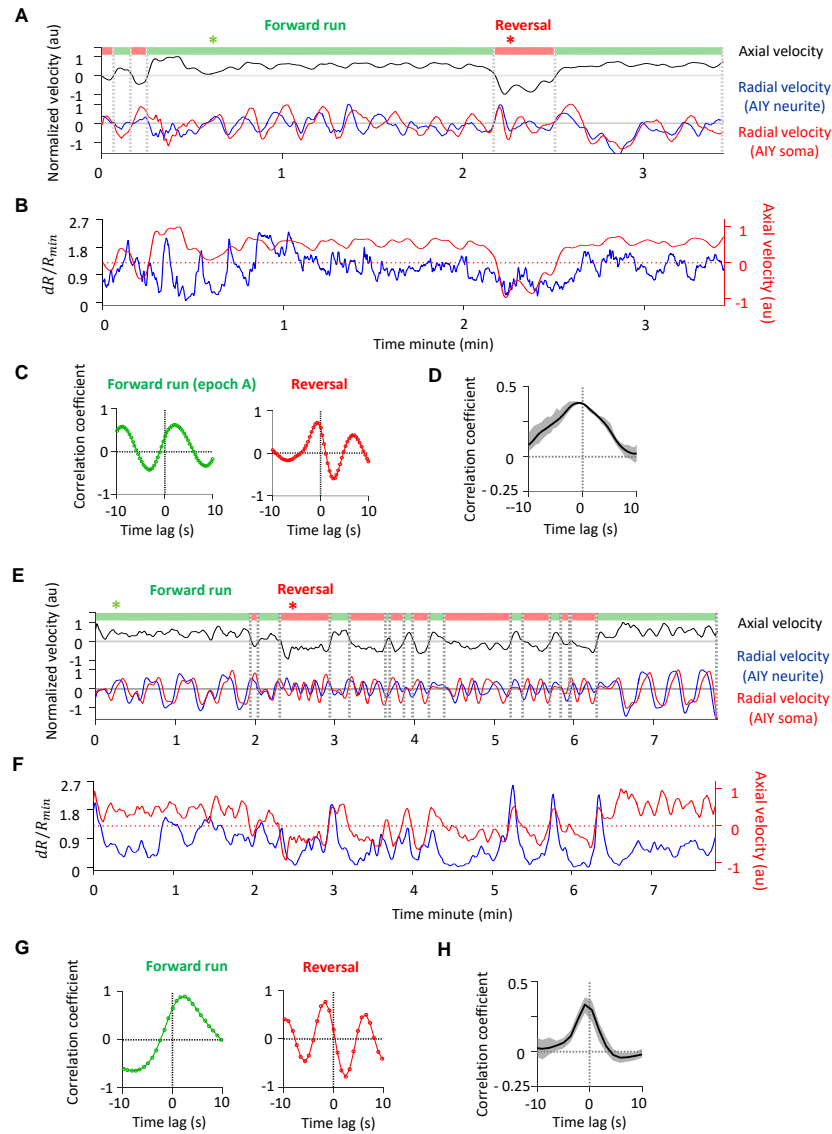
Figure 2–Figure supplement 1. Behavior state annotation in free-moving and semi-constrained animals. A-C. Annotating forward runs and reversals in a free-moving animal. **A.** Top: Locomotory state can be read out either by directly measuring the axial velocity (i.e., velocity projected onto the animal's body axis) of a landmark object (in this care, the AIY neurite, black trace), or by computing the cross-correlation of the radial velocities (i.e., component of the velocity orthogonal to the body axis) of two landmark objects located along the A-P axis (e.g., the AIY neurite (blue trace) and the more posterior AIY soma (red trace)), as illustrated in **C,D**. **B.** Calcium activity extracted from AIY neurite (blue trace) from the same recording as in **A.**, overlaid on its axial velocity (red trace, same as in **A.**). **C.** Cross-correlation functions corresponding to the forward run epoch (left panel) and the reversal epoch (right panel) marked with asterisks in **A**. During the forward run, the measured velocity of the AIY neurite precedes that of the AIY soma; the opposite is true during reversal. **D.** Average cross-correlation function between AIY calcium activity and the axial velocity of the AIY neurite, exhibiting positive correlation. Data are from N=3 wild type animals. **E-G.** Annotating forward run and reversal states in a semi-constrained animal. **E.** The axial velocity of the AIY neurite (black trace) and the radial velocities of the AIY neurite (blue) and the AIY soma (red). **F.** Calcium activity extracted from AIY neurite (blue trace) from the same recording as in **A.**, overlaid on its axial velocity (red trace, same as in **A.**). **G.** Cross-correlation functions corresponding to forward run epoch (left panel) and reversal epoch (right panel) marked with asterisks in **E**, with similar patterns as seen in textbfC.. **H.** Cross-correlation function between AIY calcium activity and the axial velocity of the AIY neurite, exhibiting positive correlation. Data are from N=5 wild type animals.
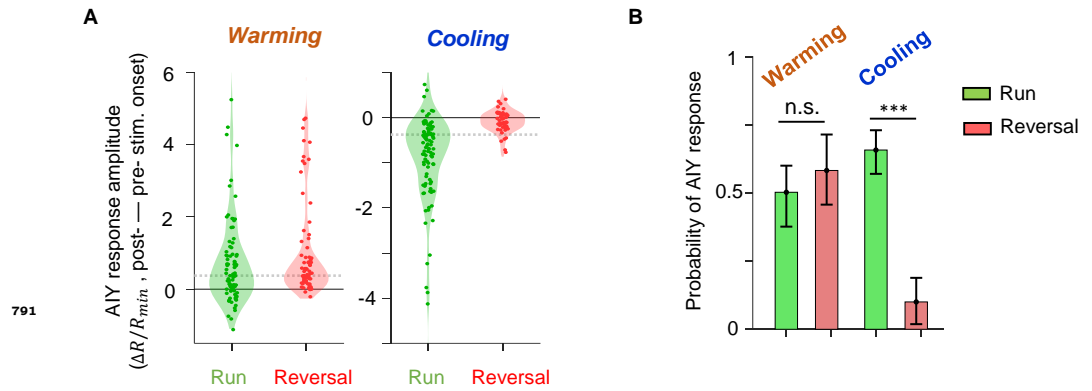
Figure 2–Figure supplement 2. Thermal response of AIY under different locomotory states
A. Violin plots showing the distribution of changes in AIY activity in response to warming (left) or cooling (right) stimuli under forward run or reversal state in wild-type animals. Dotted black lines indicate the threshold values used to calculate the response probability in **B**. **B.** Probability that the magnitude of change in AIY activity upon warming or cooling is above the defined thresholds. See **Methods and Materials** for details. For **A** and **B**, data are from N=5 wild-type animals.
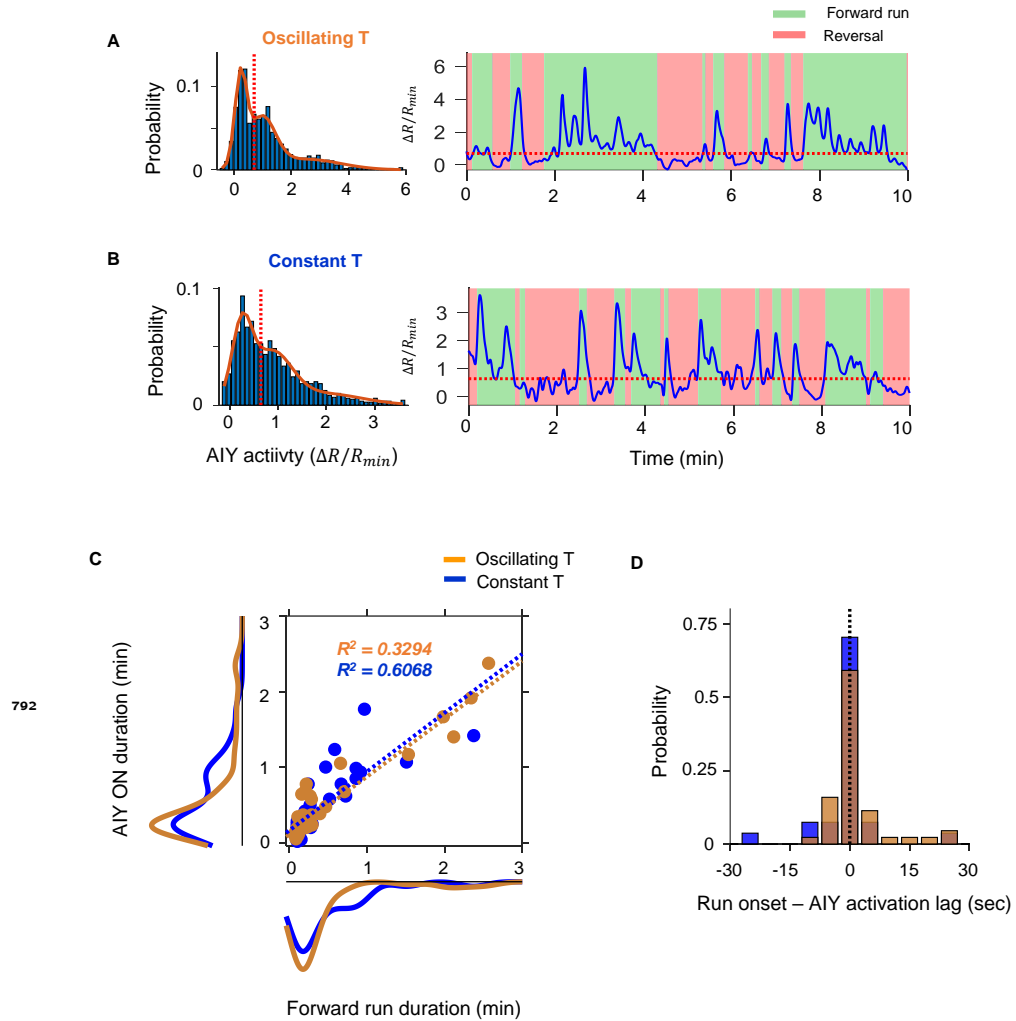
Figure 3–Figure supplement 1. Quantification of persistent activity in AIY in wild type animals. A-B. Definition of the AIY ON state. **A.** Example histogram (left) and time series trace (right) of AIY activity under oscillating temperature. Solid curve is derived by fitting the distribution with a Gaussian mixture model with 3 components. Dotted orange lines in both plots indicate the local minimum between the centers of the first two components of the Gaussian mixture model. Activity above the dotted orange line is classified as the ON state. **B.** Same analyses as in **A** on a sample AIY activity trace measured under constant temperature. Activity above the dotted orange line is classified as the ON state. **C.** The duration of the forward run state exhibits positive correlation with the duration of the AIY ON state under both oscillating and constant temperature. **D.** Time lag between the onset of AIY ON states and the onset of forward runs for data collected under oscillating (orange) or constant (blue) temperatures. Positive values indicate that the AIY ON state followed the onset of the forward run.
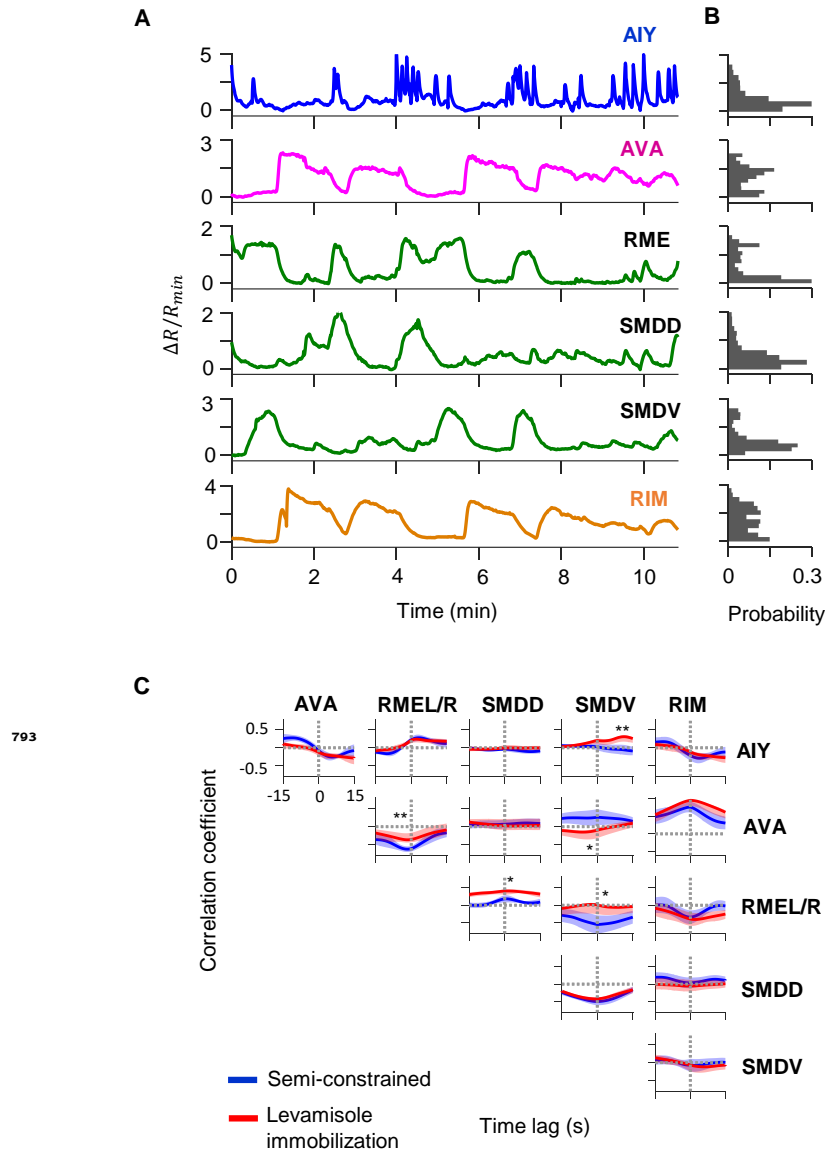
792

Figure 3–Figure supplement 2. Circuit-level neural activity in immobilized animals. A. Simultaneously measured calcium activity in AIY and neurons of the motor circuit in an animal pharmacologically immobilized by levamisole. **B.** Cross-correlation functions between the activity of AIY and that of simultaneously measured interneurons and motor neurons. **C.** Average pairwise cross-correlation functions among neurons in wild-type animals under semi-constrained (blue) and pharmacologically immobilized (red) preparations. Data are from N=4 wild-type animals. Error bars are s.e.m. Wilcoxon rank-sum test was used to compare the peak mean cross-correlation values between data under oscillating temperature versus data under constant temperature. * p<0.05; ** p<0.01; *** p<0.001; no asterisk p>0.05.
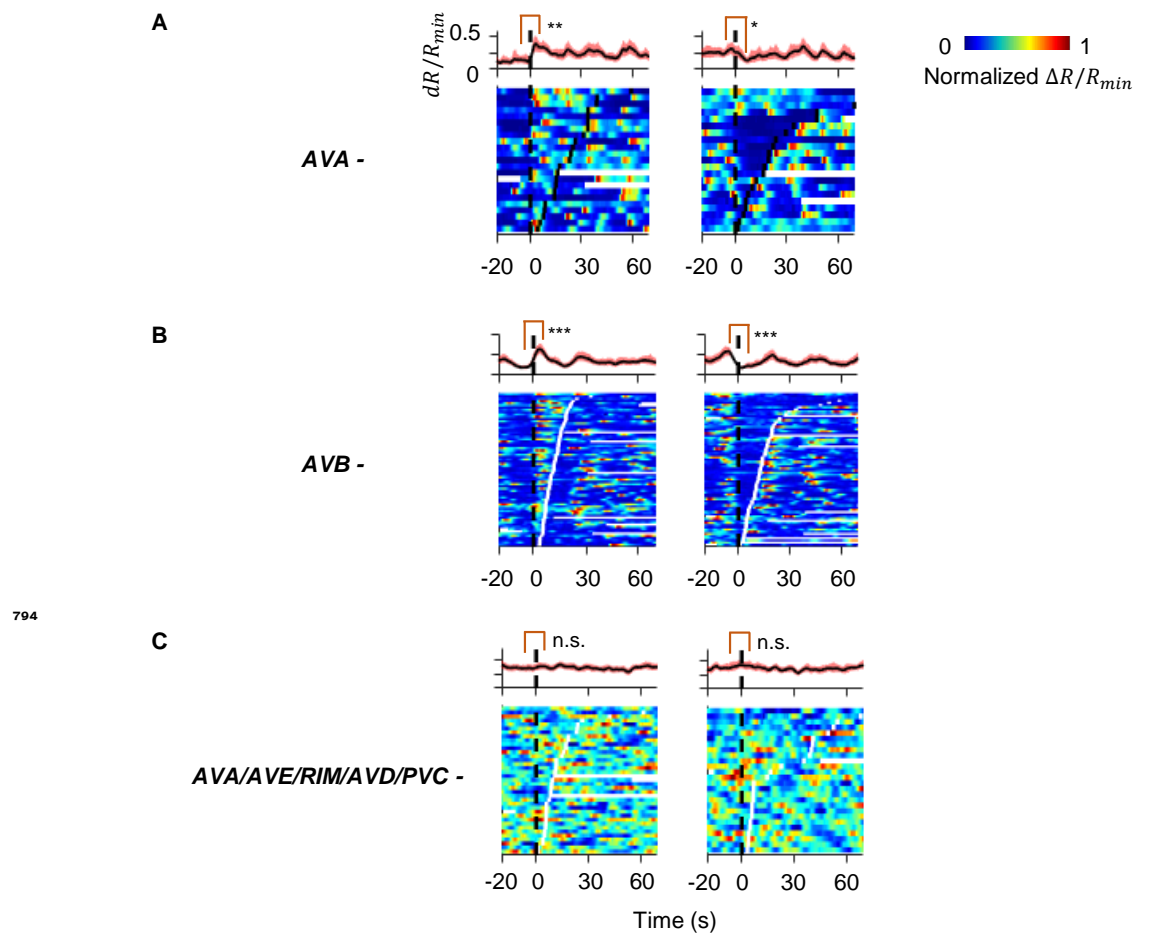
Figure 4–Figure supplement 1. AIY activity aligned to behavioral states in animals where candidate neurons for relaying the CD signal have been ablated. A. AIY activity aligned to the onset of forward runs (left column) or reversals (right column) in the animals where the AVA interneurons have been genetically ablated (N = 4). **B.** AIY activity aligned to the onset of forward runs (left column) or reversals (right column) in the animals where the AVB interneurons have been genetically ablated (N = 4). **C.** AIY activity aligned to the onset of forward runs (left column) or reversals (right column) in the animals where multiple premotor interneurons (AVA, AVE, AVD, and PVC) and the RIM neurons have been genetically ablated (N = 9).
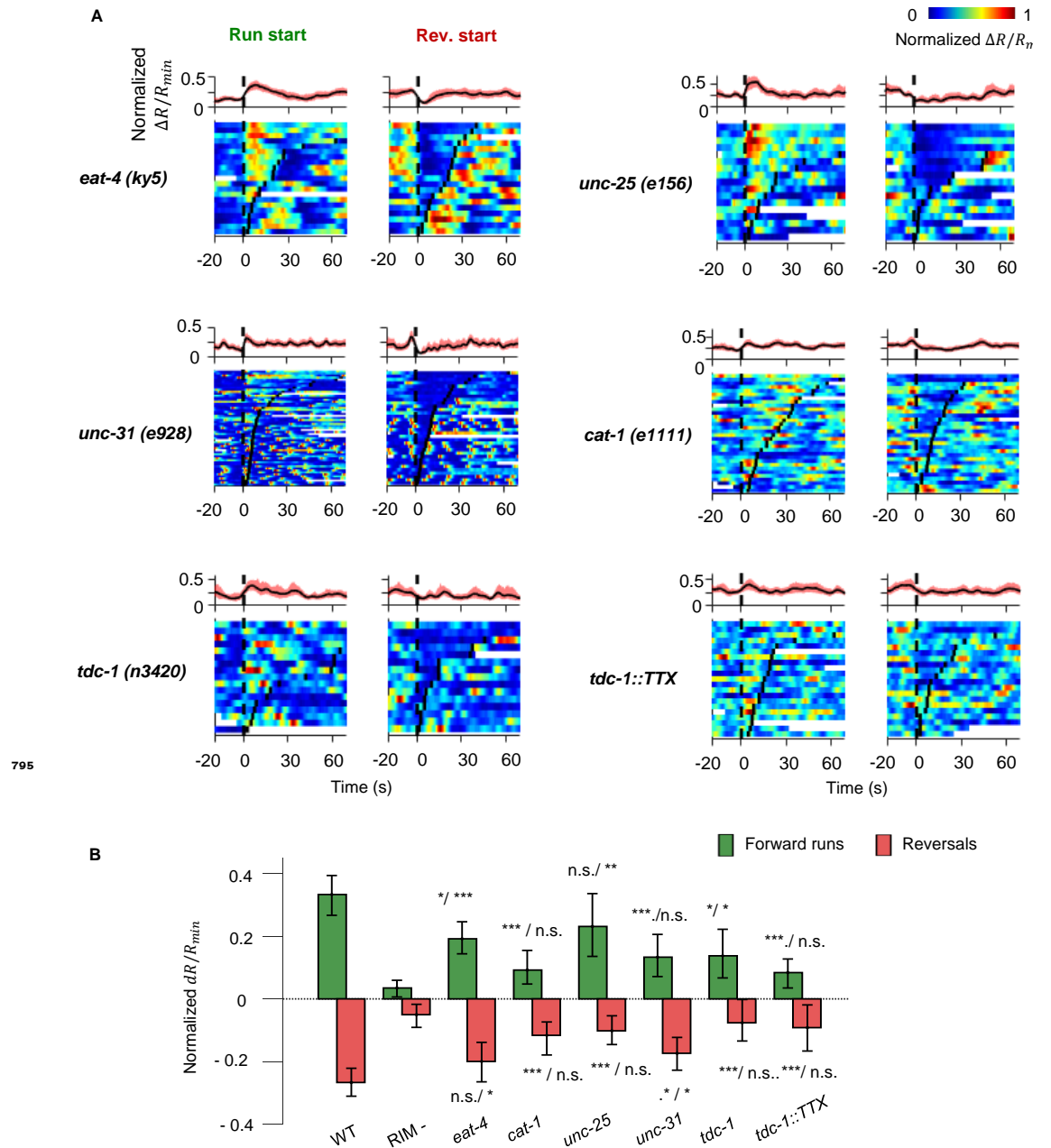
Figure 4–Figure supplement 2. AIY activity aligned to motor states in mutant and transgenic animals defective in various modes of chemical transmission. A. AIY activity aligned to the onset of forward runs (left column) or reversals (right column) in *VGLUT3/eat-4(ky5)* mutants (N=3); *VMAT/cat-1(e1111)* mutants (N=3); *GAD/unc-25(e156)* mutants (N=3); *CAPS/unc-31(e69)* mutants (N=3); *TDC/tdc-1(n3420)* mutants (N=4); transgenic animals expressing tetanus toxin (TeTx) specifically in the RIM and RIC neurons (N=4). **B.** Quantification of motor-related activity in AIY in mutants and transgenic animals presented in **A**. Significance in comparison to wild-type and to RIM ablated animals are presented side by side on top of each bar. Error bars are 95% CI. Wilcoxon rank-sum test, n.s., non-significant, * $p<0.05$; **, $p<0.01$; ***, $p<0.001$.
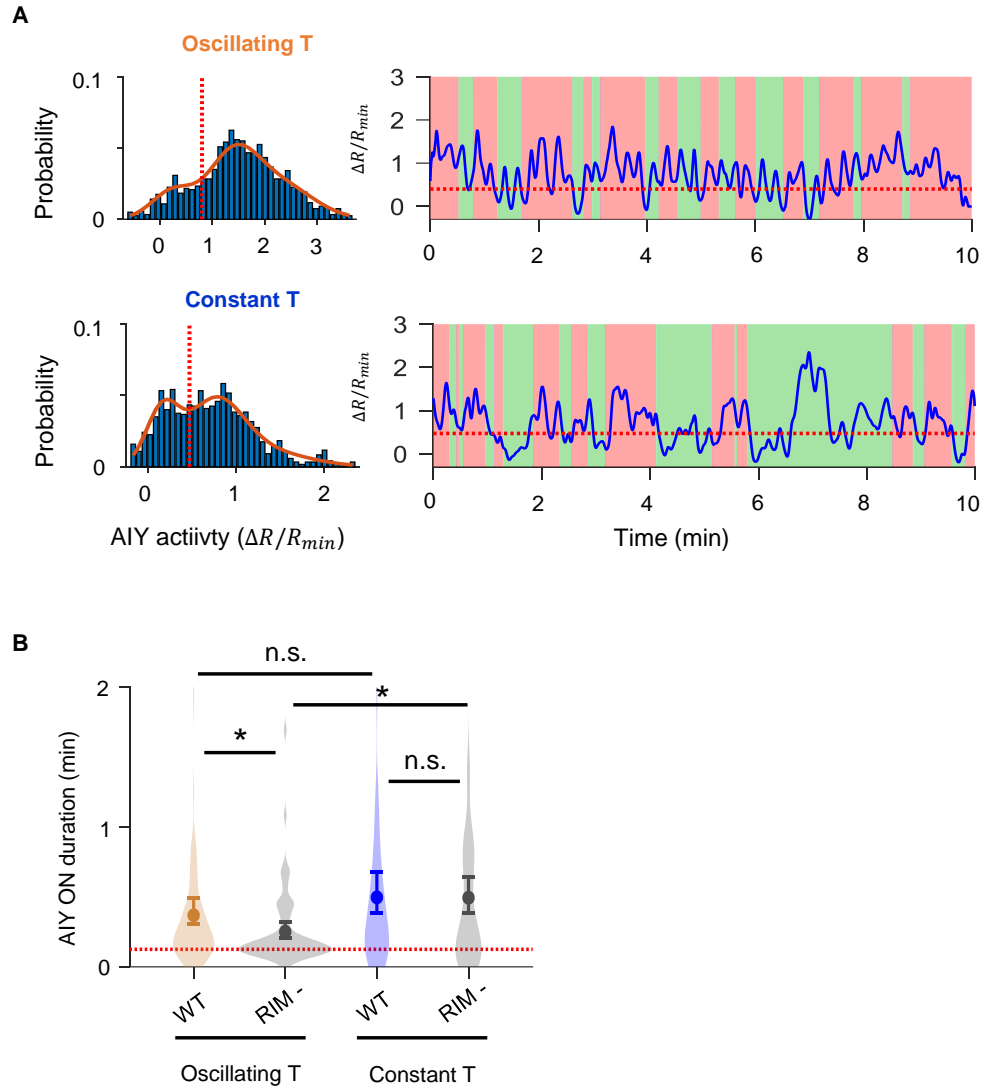
Figure 5–Figure supplement 1. Analysis of AIY activity in RIM-ablated animals. A. Top: Example histogram (left) and time series trace (right) of AIY activity under oscillating temperature. Solid curve is derived by fitting the distribution with a Gaussian mixture model with 3 components. Dotted orange lines in both plots indicate the local minimum between the centers of the first two components of the Gaussian mixture model. Activity above the dotted orange line is classified as the ON state. See **Methods and Materials** for details. Bottom: Same analyses as in **A** on a sample AIY activity trace measured under constant temperature. Activity above the dotted orange line is classified as the ON state. **B.** Violin plot showing the distributions of the duration of AIY ON states in wild-type versus RIM-ablated animals under oscillating and constant temperature. Data are from: N=5 wild-type animals under oscillating temperature, N=6 wild type animals under constant temperature, N=3 RIM ablated animals under oscillating temperature, and N=4 RIM ablated animals under constant temperature. Wilcoxon rank-sum test * p<0.05; ** p<0.01; *** p<0.001; n.s. indicates non-significant.

A. Average angular velocity of wild type (blue) and RIM ablated (gray) animals as a function of their instantaneous heading angle.

B. Average forward run durations as a function of overall run direction in wild type (blue) and RIM ablated (gray) animals.
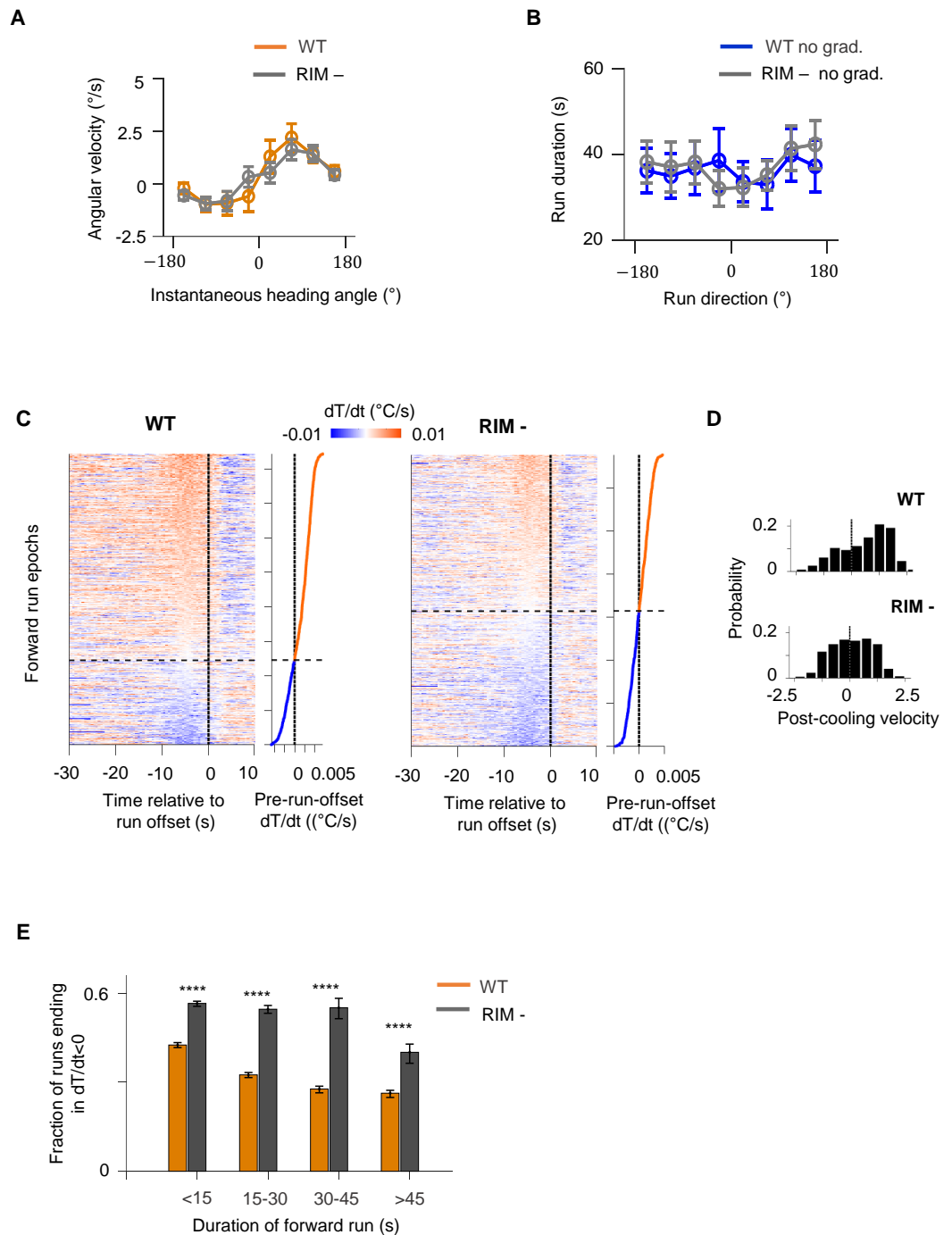
797

Figure 6–Figure supplement 1. RIM ablation results in higher likelihood of forward runs ending after a period of cooling. A. Average angular velocity of wild type (blue) and RIM ablated (gray) animals as a function of their instantaneous heading angle. **B.** Average forward run durations as a function of overall run direction in wild type (blue) and RIM ablated (gray) animals. Error bars are s.e.m. Wilcoxon rank-sum test was used to draw comparisons between wild type and RIM ablated animals. p<*0.05, **0.01, ***0.001, p>0.05 (non-significant) for panels without asterisk. **C.** Instantaneous thermal variations experienced by wild type (left) and RIM ablated (right) animals aligned to the offset of forward runs. Heat maps are generated by concatenating dT/dt time series along the y-axis, and sorting by the average dT/dt values within the last 2 seconds before the offset of forward runs (shown as line plot to the right). Black dotted lines divide instances in which forward runs ended after a period of warming from cases where runs ended after a period of cooling. **D.** Histograms of dT/dt values within the last 2 minutes before the end of forward runs in wild type (top) and RIM ablated animals (bottom). Analysis applied to same data set as in **C**. **E.** Fraction of forward runs that ended after cooling as a function of the overall duration of the forward run (orange: wild type, gray: RIM ablated).